Effect of Nano-Zinc Oxide Particles on the Performance Behavior of Waterborne Polyurethane Composite Coatings

S. K. Dhoke[1], Narayani Rajgopalan[2], A. S. Khanna[3]

Department of Metallurgical Engineering and Materials Science, Indian Institute of Technology Bombay 400076, India

[1]shailesh_zeo@rediffmail.com; [2]bnarayani@iitb.ac.in; [3]ckhanna@iitb.ac.in

Abstract- **A nano-composite coating was formed by incorporating nano-ZnO pigments in a waterborne polyurethane dispersion (WPUD) to different loading levels (0.1% and 1.0% by weight). Corrosion performance of the nano-composite coatings were evaluated by applying these nano-composites coatings on mild steel substrate and exposing them to salt-spray, humidity and accelerated UV-weathering. Mechanical properties like scratch resistance, abrasion resistance and pencil hardness were also studied. The electrochemical performance and mechanical properties of the composite coatings were evaluated using various analytical techniques. FTIR technique was used to investigate the interaction between nano-ZnO particles and the polymer functionalities. SEM and AFM were used to investigate dispersion of nano-ZnO particles and the changes in the surface behavior of the modified coatings before and after exposure to the test environment. The optical property of the coating was evaluated using UV-Visible spectrophotometer. The results showed an improvement in the corrosion, UV and mechanical properties of the coatings at lower concentration (0.1% by wt), indicating the positive effect of addition of nano-ZnO particles in the coatings. It was found that the optical transparency of the coating was not altered at lower loading level of nano-ZnO particles.**

Key Words- Waterborne; Polyurethane; Nano-Zno; Corrosion Resistance; UV Resistance

I. INTRODUCTION

An aqueous polyurethane dispersion is a binary colloid system in which polyurethane particles are dispersed in a continuous aqueous medium [1, 2].The basic building blocks of solvent borne polyurethanes like diisocyanates, polyols, amines catalysts and additives are common to aqueous based system as well [3]. Though, the development of aqueous polyurethane dispersions was motivated primarily by environmental considerations, one technical advantage of aqueous polyurethane dispersion is that the viscosity of dispersion is independent of the molecular weight of polymer. Thus, polyurethane dispersion can be prepared at a high solid content with a molecular weight high enough to form films with excellent performance solely by physical drying [2]. Economical aspect is another reason as they do not contain the expensive solvents [3]. Compared to their solvent counterparts, polyurethane dispersions can offer the following advantages: viscosity and flow properties independent of molecular weight, the absence of external emulsifiers, environmental safety, good adhesion, and rheology characteristics [4]. Other advantages which make them attractive as waterborne coatings are the outstanding properties of solvent, stain, chemical resistance, toughness with flexibility [5].

With the quest for new developed coating systems with better performance, aqueous based polyurethane coatings are modified with various nano-particles [6-13]. Nanotechnology presents a wide range of opportunities to improve performance of coatings and promises to deliver breakthrough performance specifically with respect to scratch and mar resistance, barrier properties including corrosion resistance and mechanical properties [14, 15]. Optical clarity is one of the many features of nano-particles, extremely important in expanding nano-particle applications in coatings. They can be added to a clear coating formulation with little or no adverse impact on visual characteristics. Nano-particles most commonly used in coatings are SiO2 [7, 11, 12, 13], TiO2 [16], ZnO [6, 8, 9, 17], Al2O3 [18.19], Fe2O3 [20] and CaCO3 [21]. Use of nano-particles are most commonly based on the inherent properties they posses. For example nano-titania and nano-zinc oxide are most commonly used as UV blocking agents, whereas nano-alumina and nano-silica are used to improve scratch and abrasion resistance of the coating. The enhanced properties are result of the much greater surface to volume ratio of the nano-pigment that is often characterized by very high aspect ratios [23].

Present study refers to the effect of addition of nano-zinc oxide on water-borne polyurethane coating system at two different loading levels (0.1% and 1.0% by weight). The nano-modified coatings were applied on pretreated mild steel panels by dip coating techniques. Dip coating techniques can be described as a process where the substrate to be coated is immersed in a liquid and then withdrawn with a well-defined withdrawal speed under controlled temperature and atmospheric conditions. The coating thickness is mainly defined by the withdrawal speed, by the solid content and the viscosity of the liquid. Dip coating was used keeping into view the industrial viability of the coating. Using this technique uniform film can be applied onto flat and cylindrical substrates with ease and high production rates and high transfer efficiency. The process is cost effective and requires low labor as compared to other application process. The performance behavior of the nano-particle modified coating systems with respect electrochemical, UV resistance and mechanical properties was investigated.

II. EXPERIMENTAL

A. Material Used

Nano-ZnO with a mean size of 35 -40 nm and specific area of 29 m2g-1 was procured from Horsehead Corporation Company (USA). A one pack water-borne polyurethane dispersion (WPUD) based on aliphatic urethane was procured from Dooall Corporation Pvt. Ltd, India.

B. Preparation of Nano-Particle Modified Polyurethane Waterborne Coating

Waterborne polyurethane dispersion (WPUD) was stabilized with nano-zinc oxide pigments in different concentrations by Ultrasonic probe dispersion equipment for about 45 minutes until a clear coat was obtained. The nano-modified coating system thus formed was applied on pretreated cold roll milled steel panels by dip-coating. Pre-treated mild steel substrates were immersed in the solution of the coating material at a constant speed and held in coating bath for a while. The substrate was pulled up from the bath while the thin layer of the coating deposits itself on the substrate. The excess coating dripping from the substrate was wiped off and the coating was allowed for oxidative curing at room temperature for 24 hours. The coating thickness was found to be 10 µm. The coated panels were used for electrochemical and mechanical characterizations.

III. RESULTS AND DISCUSSION

A. Characterization of Nano-Composite Coating

The interaction of nano-particles with base matrix was investigated using Fourier transform infra-red spectroscopic (FTIR, Nicolet Magna 550 FT-IR spectrometer). Electrochemical behavior of the coating was investigated by exposing the test panels to Salt Spray (ASTM B117), Humidity (ASTM D2247) and UV weathering (ASTM G53). Mechanical properties were studied by Scratch (BS.3900), Taber abrasion (ASTM D4060) and pencil hardness (ASTM D-3363-05) methods. Optical property was studied using UV-Vis spectrophotometer (Shimadzu UV-160A) surface morphological studies were carried out using Scanning Electron Microscopy (SEM, Model no.S3400, Hitachi) and Atomic force microscopy (AFM, Digital Instrument Nanoscope IV).

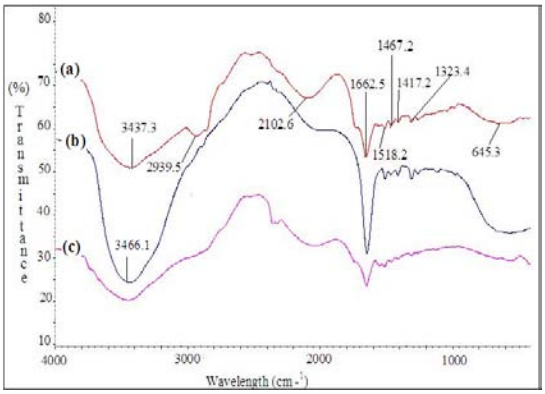

Fig. 1 Shows the FT-IR spectra of (a) Neat-WPUD and WPUD modified with (b) 0.1% nano-ZnO and (c) 1.0 % nano-ZnO.

B. Fourier Transform Infra-Red Spectroscopic (FTIR) Analysis

Fig. 1 shows the overlay FTIR spectra of neat-WPUD coating and nano-ZnO modified composite coatings. The functional groups corresponding to the particular frequencies are given in Table Ⅰ and Table Ⅱ respectively. From (Fig. 1a) N-H stretching in neat WPUD is observed at 3437.3 cm-1, while in WPUD modified with 0.1 % nano-ZnO, the N-H stretching peak lies at slightly higher value of 3466.1 cm-1(Fig. 1b). The probable reason for this shift is attributed to hydrogen bonding between N-H and free NCO groups in neat -WPUD. After adsorption of WPUD on nano-ZnO surface, the hydroxyl groups on nano-ZnO gets hydrogen bonded with NCO groups on WPUD. Thus, N-H groups are constrained by nano-ZnO surface and thus cannot form hydrogen bonds. Therefore, N-H stretching appears at a higher frequency in IR spectrum and on other hand, N-H group can easily find a carbonyl group to form hydrogen bonds to stabilize the system. It thus suggests a strong interaction between polymer and nano-ZnO particle [8]. Similar results were obtained for WPUD modified with 1.0% nano-ZnO. (Fig. 2c). Also, reduction of peek intensity at 2939.5 cm-1 (C-H stretching in neat-WPUD) in modified coating indicates the interaction of nano-particle surface with the polymer functionality.

TABLE I BAND ASSIGNMENT FOR NEAT-WPUD

Band (cm^{-1})	Assignments
2939.5	C-H Stretching
3437.3	N-H Stretching Due to Hydrogen Bonding
1662.5	C=O Stretching
1323.4	C-N Stretching

TABLE Ⅱ BAND ASSIGNMENT FOR NEAT-WPUD MODIFIED WITH NANO-ZNO PARTICLES IN DIFFERENT CONCENTRATIONS

Band (cm-1)	Assignments
3466.1	N-H Stretching (Free) i.e. without Hydrogen Bonding
1662.5	C=O Stretching
1316.2	C-N Stretching

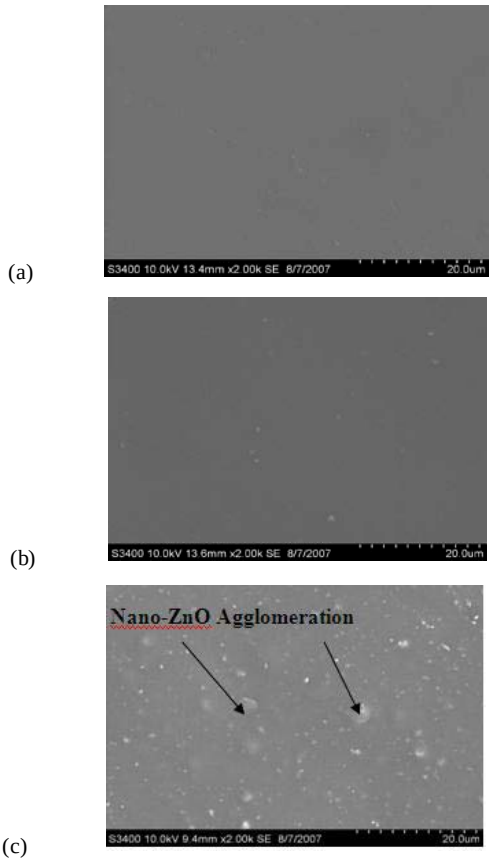

Fig. 2 SEM surface micrographs of unexposed samples: (a) Neat-WPUD, (b) WPUD + 0.1% nano-ZnO and (c) WPUD + 1.0 % nano-ZnO

IV. ELECTROCHEMICAL ANALYSIS

Fig. 2 shows the SEM micrographs of neat-WPUD coating and coating modified with nano-ZnO particles in different loading levels, before exposure to the test environments. From Fig. 2a, it can be clearly seen that the coating formed is uniform and free from heterogeneity on the surface. After modifying WPUD with nano-ZnO particles, the coating modified with 0.1% nano-ZnO particles (Fig. 2b) show uniform surface morphology indicating proper dispersion of nano-particles, while the surface micrograph of coating modified with 1.0 % nano-ZnO particles (Fig. 2c) show white spots all over the surface indicating agglomeration of the nano-particles.

Fig. 3 shows the surface micrographs of the neat WPUD and nano-composite coatings after 800 hours of exposure in salt spray chamber. From Fig. 3a, it can be seen that the coating degradation after exposure to salt spray is more distinct in neat sample than those modified with nano-ZnO particles, indicating that the neat WPUD coating has undergone chemical changes during exposure. However, the performance was better for the coating modified with 0.1% nano-ZnO (Fig. 3b) than for coating modified with 1.0 % nano-ZnO (Fig. 3c). At lower loading level, the concentration of nano-ZnO particle is so small that the well-disperse particles in the coating restricts the diffusion of the corrosive electrolyte through the coating film acting as an effective barrier. It may be attributed that for lower loading level of nano-ZnO, the well-dispersed particle having large surface area and small size absorb more resin on its surface which enhances the density of the coatings thereby reducing the transport paths for the corrosive electrolyte to pass through the coating and consequently reducing the corrosion process [9, 24, 25]. At higher loading level the increase in the number of particles form agglomerates because of their high surface activity introducing defect in coatings. These defects act as site for electrochemical reaction affecting the coating performance. AFM topographic images for salt-spray exposed samples for 800 hours also provide the same information (Fig. 4). As can be seen from Fig.4a, the surface of neat sample is completely heterogeneous as compared the surface of coatings modified with nano-ZnO particles (Fig. 4b and Fig. 4c), which show a little change on the surface appearance, indicating better protection.

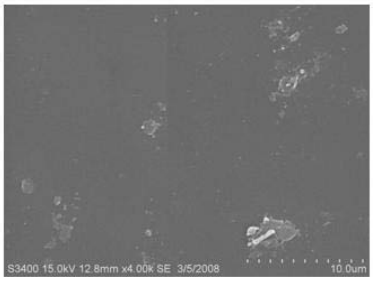

(a)

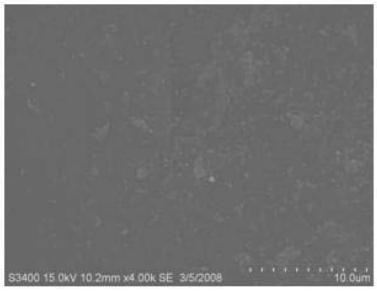

(b)

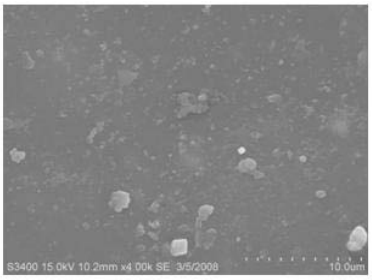

(c)

Fig. 3 SEM micrographs of salt-spray exposed samples: (a) Neat-WPUD, (b) WPUD + 0.1% nano-ZnO and (c) WPUD + 1.0 % nano-ZnO

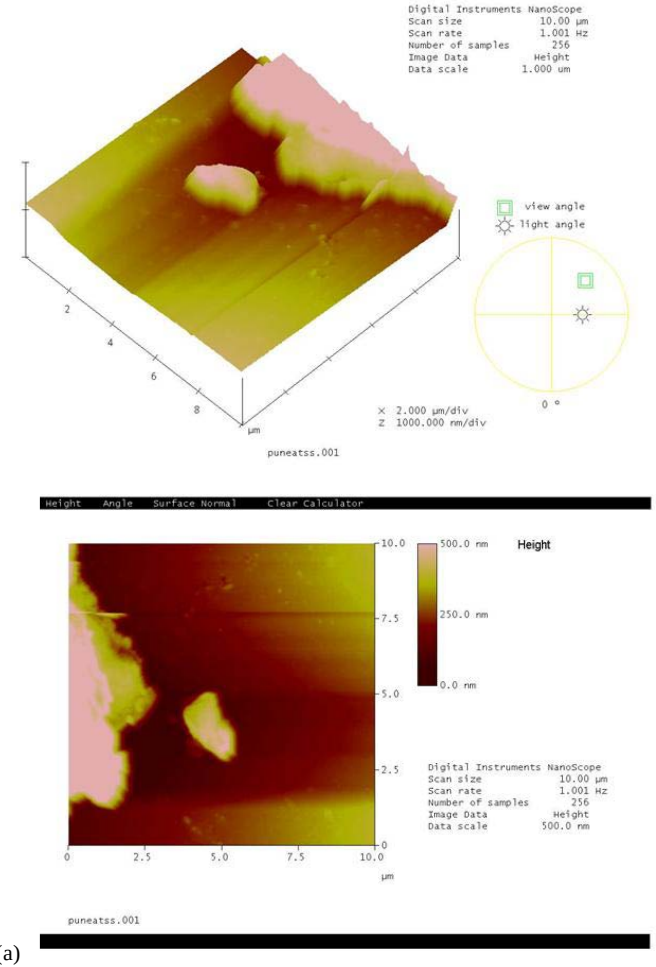

(a)

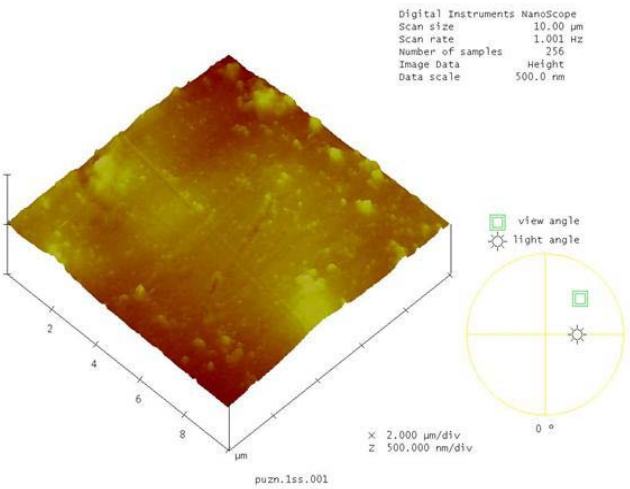

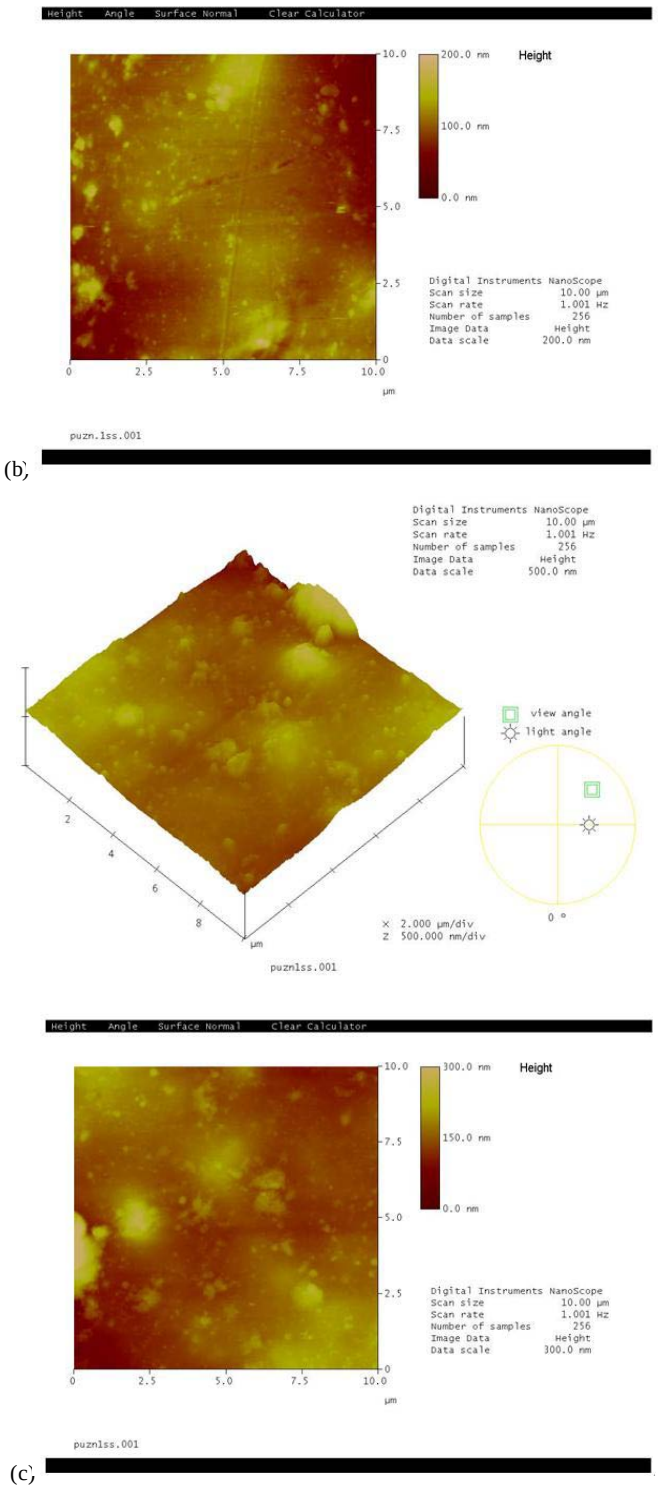

Fig. 4 AFM topographic height images of Salt-spray exposed coating surface at a scan size of 10µm x 10µm (a) Neat-WPUD, (b) WPUD + 0.1% nano-ZnO and

(c) WPUD + 1.0 % nano-ZnO

Fig. 5 shows the SEM micrographs of humidity exposed samples for 1000 hrs. The surface micrograph of the neat sample (Fig. 5a) shows presence of blisters all over the surface. This indicates that the coating has undergone drastic changes during exposure leading to the failure. With the incorporation of nano-ZnO pigment in the coating system, no such defects were observed. Fig. 5b and Fig. 5c represent the SEM surface micrographs of the coating modified with nano-ZnO particles at different concentrations respectively. As can be seen from the SEM micrographs (Fig. 5b) coating at lower loading level (0.1%) appears more uniform and devoid of areas of delamination, degradation and blisters. This again can be attributed to proper pigment concentration and dispersion in the polymer matrix. Also, the interaction of the nano-ZnO with the polymer is strong, whereby the strongly bounded interface does not allow the permeation of water. However, at higher loading level some pinholes and other heterogeneities are clearly observed at the agglomerated sight (Fig. 5c). AFM topographic height images (Fig. 6) for humidity exposed samples also provide the parallel observations. Fig. 6a represents AFM image of neat samples showing completely distorted surface, indicating changes in the surface roughness and microstructure of the coating. Coating system with lower concentration of nano-ZnO particles (0.1% by wt) show little change in the surface roughness and microstructure of the coating (Fig. 6b) as compared to the coating system (Fig. 6c) with higher loading level (1.0 % by wt), suggesting the improvement in the humidity resistance of the coating.

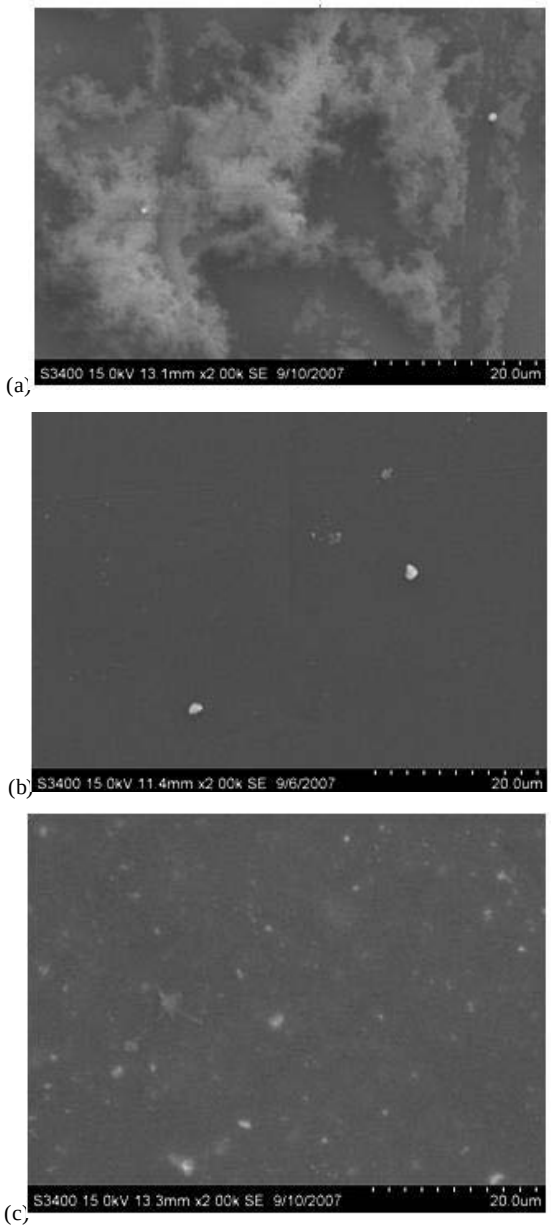

Fig. 5 SEM micrographs of humidity exposed samples: (a) Neat-WPUD, (a) WPUD + 0.1% nano-ZnO and (c) WPUD + 1.0 % nano-ZnO

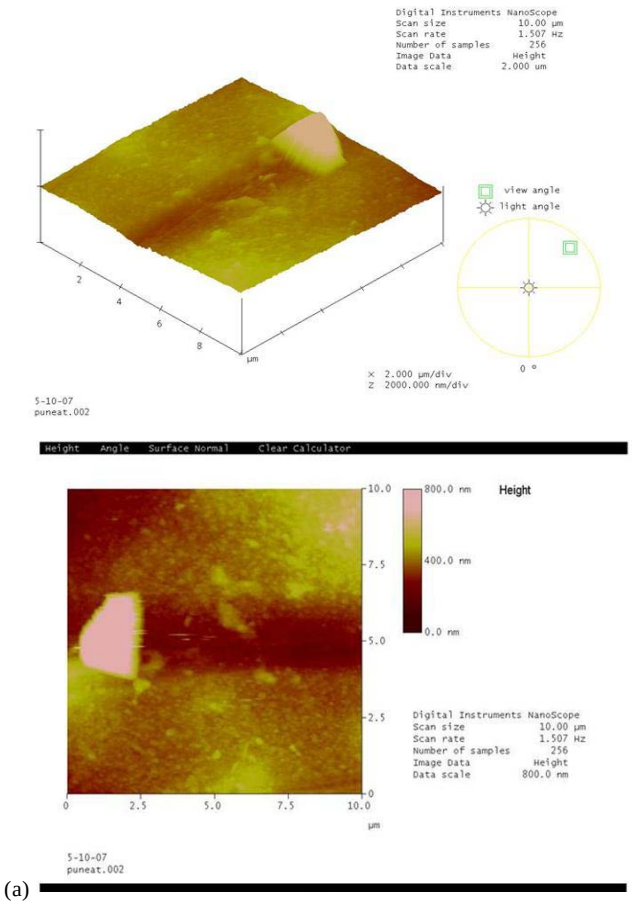

(a)

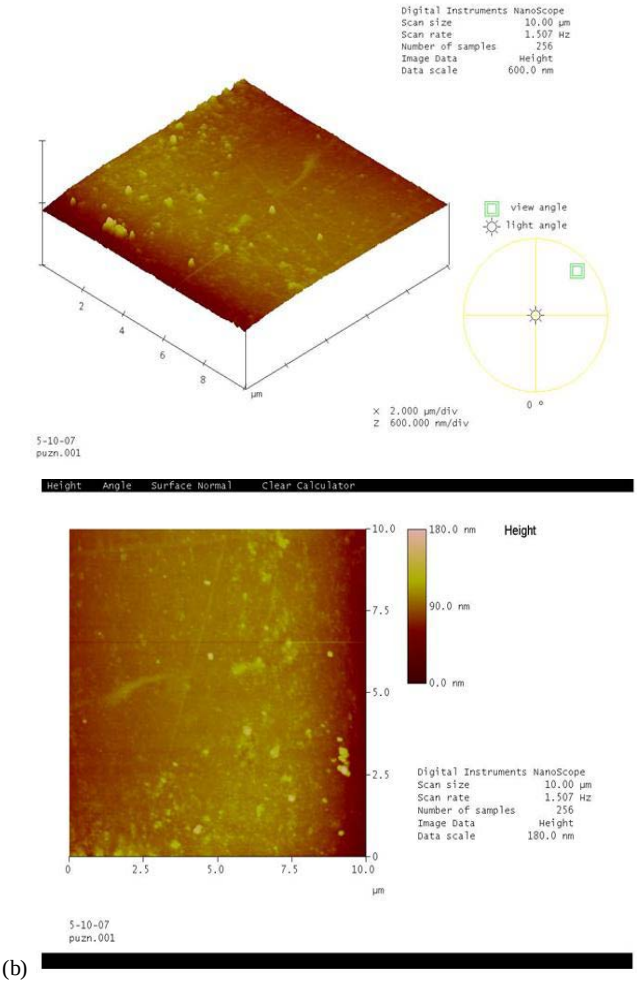

(b)

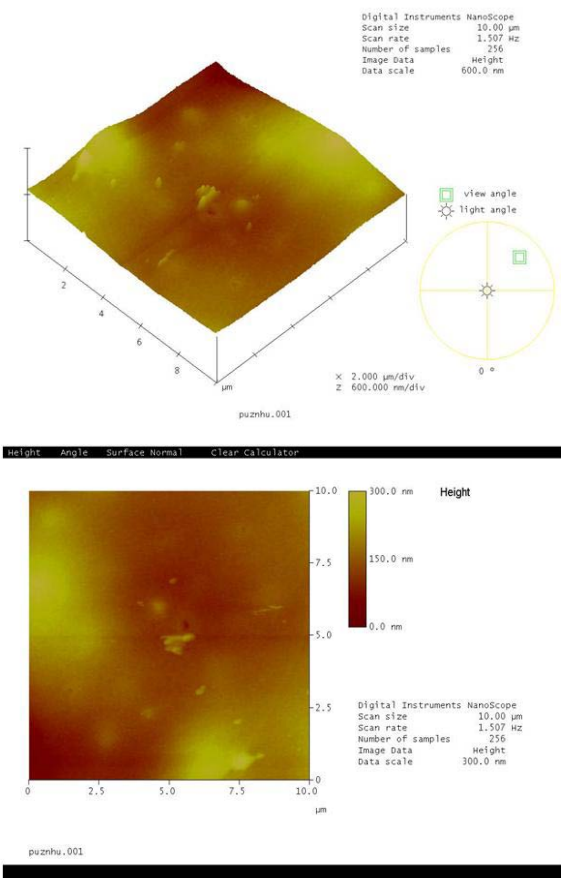

(c)

Fig. 6 AFM topographic height images of humidity exposed coating surface at a scan size of 10µm x 10µm: (a) Neat-WPUD, (b) WPUD + 0.1% nano-ZnO and

(c) WPUD + 1.0 % nano-ZnO

Fig. 7 shows the surface micrographs of UV exposed samples after 1000 hours, where the source of irradiation used was UV-B lamp which emits wavelength of 313 nm. The degradation of coating due to photo-chemical interaction is distinctly observed in neat- WPUD coated sample. The presence of surface heterogeneity clearly indicates the degradation of coating due to long term exposure to UV radiation (Fig. 7a). The coating modified with nano-ZnO showed an improvement in the UV resistance. No changes were observed for the coating modified with 0.1% of nano-ZnO (Fig. 7b). However, for coating modified with 1.0 % of nano-ZnO (Fig. 7c) appearance of pin-holes are clearly observed. This suggests that, though the induction time for surface degradation is delayed, the performance of the coating was inferior as compared to the coating modified with lower concentration of nano-ZnO. The improvement of UV resistance of the modified coating can be attributed to the fact that, nano-ZnO has a wide band gap (3.37 eV) and large excitation binding energy of 60 meV, therefore it can absorb light that matches or exceeds their band gap energy and which lies in the UV range of the solar spectrum [26, 27] . Thus, a well dispersed nano-ZnO particles attenuate UV radiations and protects the polymer matrix from degradation. Fig. 8 shows the AFM topographic height image of UV exposed samples. For Neat-WPUD coating the surface appears to be more heterogeneous with increased roughness, indicating surface degradation (Fig. 8a). Coating with 0.1% nano-ZnO shows effective improvement in UV blocking properties (Fig. 8b). It can be attributed that the small surface area per unit mass and volume increases the effectiveness of the blocking

UV radiation and prevent photo-degradation of base polymer matrix. Also, nano-ZnO due to their ceramic nature are inherently stable [28] and at this dimension posses lower photochemical activity [29] thereby providing good UV blocking property to the coating system without interacting with the UV radiation. However, the performance of nano-ZnO at higher loading level is not satisfactory, as presence of pinholes and cracks are clearly seen (Fig. 8c) due to formation of agglomeration in the coating matrix.

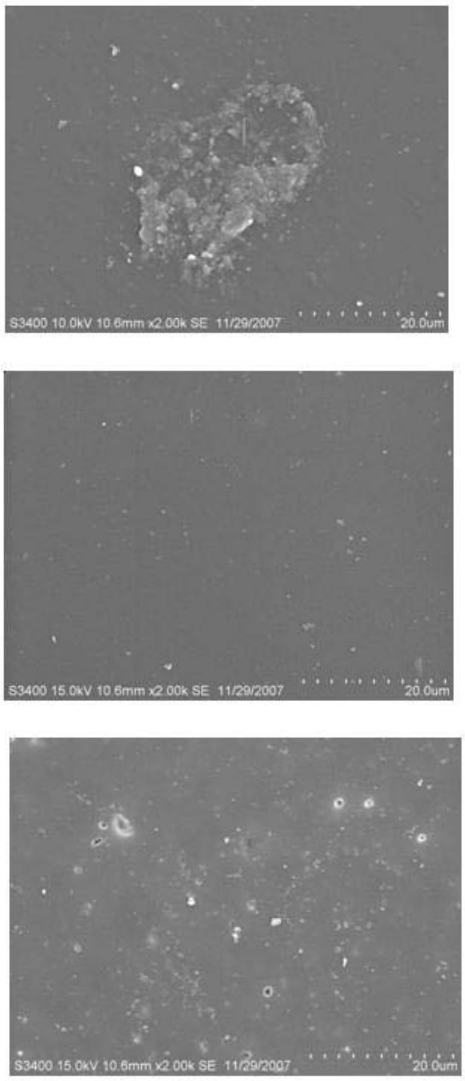

(a)

(b)

(c)

Fig. 7 SEM micrographs of UV exposed samples: (a) Neat-WPUD, (b) WPUD + 0.1% nano-ZnO and (c) WPUD + 1.0 % nano-ZnO

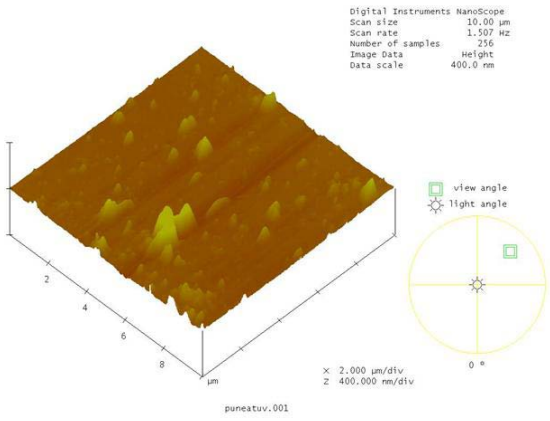

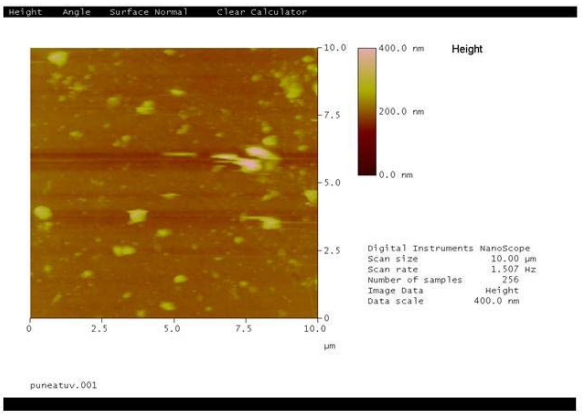

(a)

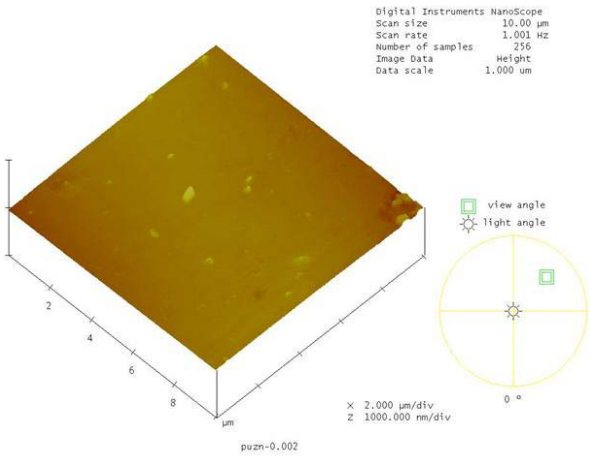

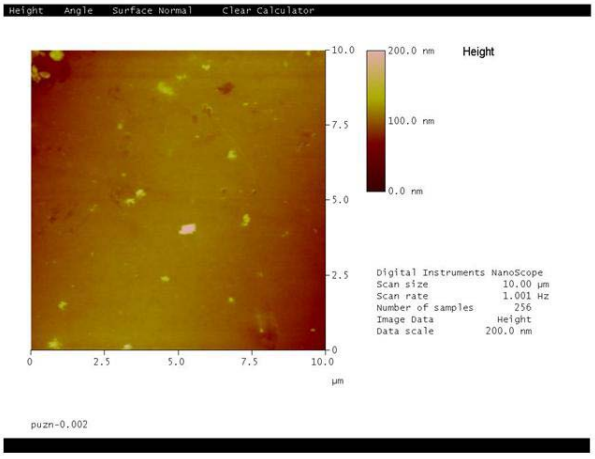

(b)

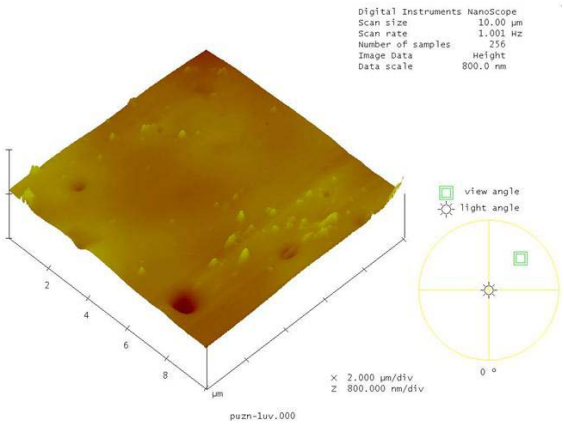

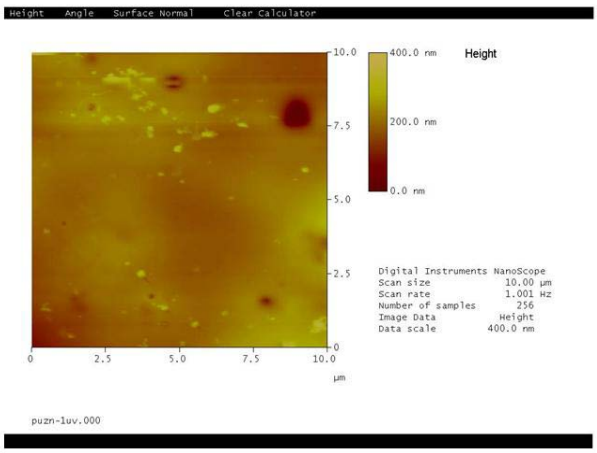

(c)

Fig. 8 AFM topographic height images of UV exposed coating surface at a scan size of 10µm x 10µm: (a) Neat-WPUD, (b) WPUD + 0.1% nano-ZnO and (c) WPUD + 1.0 % nano-ZnO

V. AFM SURFACE ROUGHNESS ANALYSIS

Table III represents the surface roughness values for neat-WPUD and nano-ZnO modified WPUD coating system before and after exposure to the test environment. After exposure to various test environments it was found that the surface roughness of neat sample is higher due to breakdown of polymer matrix as compared to the surface roughness of nano-particle modified coating. This suggests the improvement in the properties of the coating after modification. However, the surface roughness of coating modified with 0.1% nano-ZnO was relatively less then the coating modified with 1.0 % nano-ZnO, suggesting that for a higher loading level of nano-particles the resin available is not sufficient to fill all inter-pigmentary interstice leading to porous film with inferior corrosion resistance.

TABLE III AFM SURFACE ROUGHNESS VALUES (NM) MEASURED FOR COATINGS EXPOSED TO SALT SPRAY, HUMIDITY AND UV RADIATION

Test	Neat-WPUD	WPUD + 0.1% Nano-Zno	WPUD + 1.0% Nano-Zno
Salt Spray	128.66 nm	22.00 nm	34.04 nm
Humidity	132.71 nm	14.55 nm	46.24 nm
UV-Weathering	20.54 nm	13.00 nm	23.00 nm

VI. OPTICAL STUDY

Fig. 9 shows the transmittance spectra of neat-WPUD and nano-ZnO modified WPUD. From the graphs it can be seen that the transmission values for the neat-WPUD and WPUD modified with 0.1 % nano-ZnO particles are ranged between 80%-95%. This indicates that the transparency of the coating system is not much affected on addition of nano particles, supporting the fact that nano-particles do not affect the clarity of the coatings. This may be because of the fact that, particles in nano-dimension are smaller than the wavelength of visible light and so no scattering and reflecting occurs in the visible light range leading to transparent nano-composite [30]. However, the transmittance value for WPUD modified with 1.0% nano-ZnO particles is ranged between 50-60 %. This is due to formation of agglomerates of nano-ZnO particles that protrude out on the film increasing the surface roughness of the coating resulting into reduced optical transparency of the coating.

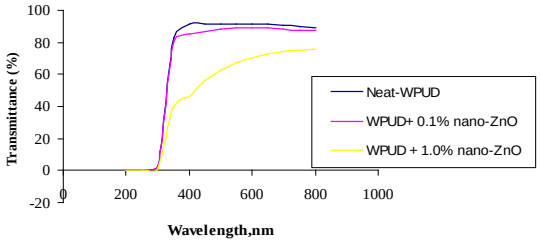

Fig. 9 Transmittance spectra of neat-WPUD and nano-ZnO modified WPUD in different concentrations as labeled

VII. MECHANICAL CHARACTERIZATION

A. Scratch Resistance

Fig. 10 shows the variation of load (weight in grams) with different concentartion of ZnO nano-particles during scratch test. From the graph it can be seen that the neat-WPUD coating is resistant to scratch at a load of 700 gm, while nano-ZnO modified WPUD coated sample showed resistance to scratch at loads of 1100 gm and 900 gm for 0.1% and 1.0% loading levels, respectively. The improvement in the scratch resistance of the coating at lower level (0.1 % by wt) can be attributed to the strong bonding network between functionalities of polyurethane and nano-ZnO particles along with their propre dispersion, which provides more resistance to scratch causing less deformation in the sample [31]. The decrease in the scratch resistance at higher loading (1.0 % by wt) may be attributed to the heterogeneities in the coating system due to aggregate formation that remained poorly dispersed in the matrix, causing inferior bulk properties at higher loadings.

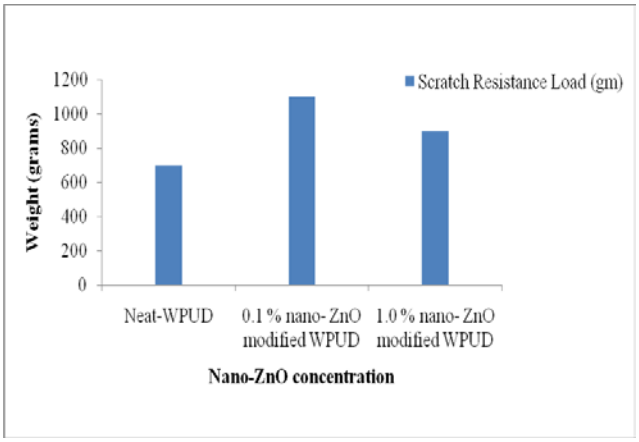

Fig. 10 Effect of the nano-ZnO concentration on the scratch resistance of WPUD

B. Abrasion Resistance

Taber Abrasion test was carried out to determine the abrasion resistance of coating. Depending upon the thickness of the coating, a specified number of revolutions was performed (1000 cycles) with all coated samples. Fig. 11 shows the SEM micrographs of taber abraded coatings. It can be seen from Fig. 11a, that the coating systems without nano-ZnO are completely wearied with more distorted surface morphology indicating poor response to abrasive action. With

incorporation of nano-ZnO particles, the improvement in abrasion resistance of the coating was observed. Coating modified with 0.1% nano-ZnO (Fig. 11b) showed better abrasion resistance then the coating modified with 1.0 % nano-ZnO (Fig. 11c). The differences in the coating performance are related to the dispersion state of the nano-particles and the volume fraction of the polymer surrounding the particles. For coating modified with 0.1% of nano-ZnO, it may be attributed that strong surface interaction between the dispersed nano-ZnO surface and polymer matrix results into compact coating providing strength against abrasive action. However, for coating with 1.0 % loading of nano-ZnO, the formation of aggregates decreases the effective surface area of the particle, which in turn decreases the volume fraction of the interphase region. Agglomerate formation in coating introduces defects which act as preferential sites for crack initiation leading to abraded surface morphology indicating poor abrasion resistance [31].

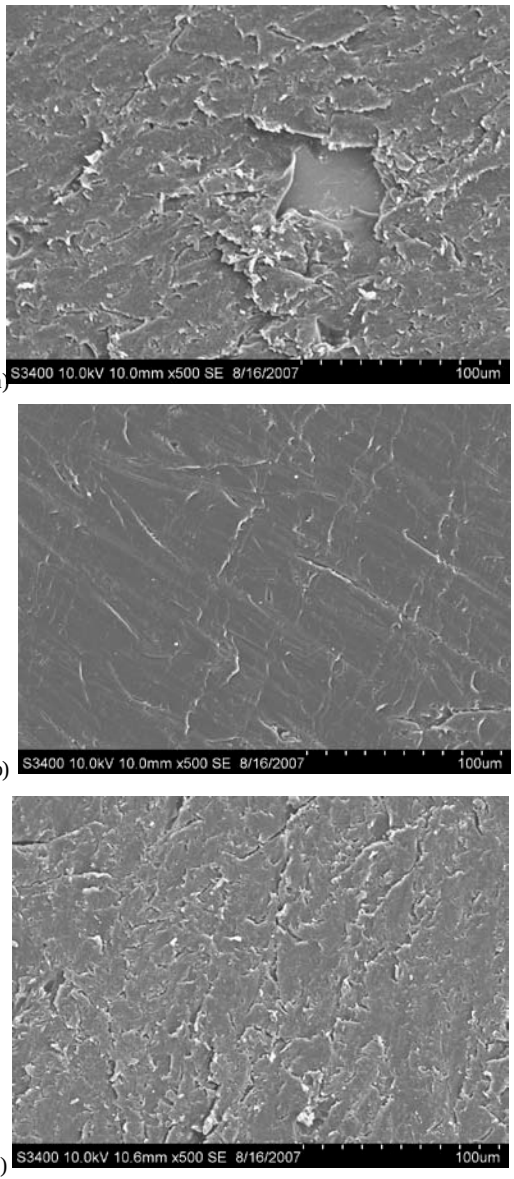

Fig. 11 SEM micrographs of abraded coating (a) Neat-WPUD and modified with (b) 0.1% nano-ZnO and (c) 1.0 % nano-ZnO

C. Pencil Hardness

Pencil hardness test was carried out for neat-WPUD and nano-ZnO modified WPUD (Fig. 12). Pencil hardness for the neat-WPUD coated sample was found to be 3H. With addition of nano-ZnO particle, the hardness of the coating was enhanced, the grade being 5H at the lower loading level (0.1%) and 4H at higher loading level (1.0%).

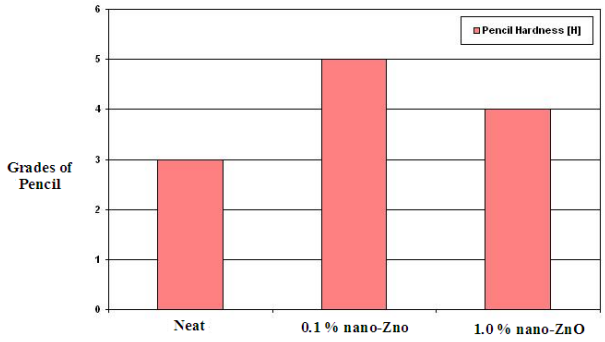

Fig. 12 Pencil hardness test

VIII. CONCLUSION

The effect of nano-ZnO particles on waterborne polyurethane dispersion (WPUD) was studied. The nano-composite coating modified with 0.1% nano-ZnO enhanced corrosion resistance, UV resistance and mechanical properties maintaining its optical transpernacy, as compared to the coating modified with 1.0 % nano-ZnO. Nano-ZnO can serve as a good barrier pigment and UV blocking agent in WPUD, however optimizing their concetration and improved dispersion in polymer matrix can further improve the performance properties of the coating.

REFERENCES

[1] B. K. Kim, Aqueous polyurethane dispersions, Colloid Polymer Science, 274 (1996) 599-611.

[2] M.G.Lu, J.Y.Lee, M.J.Shim, S.W.Kim, Synthesis and properties of anionic aqueous polyurethane dispersions, Journal of Applied Polymer Science, 86 (2002) 3461-3465.

[3] Karl-Ludwig Noble, Waterborne polyurethanes, Progress in Organic coatings, 32 (1997) 131-136.

[4] Richard G. Coogan, Post-cross-linking of water-borne urethanes, Progress in Organic coatings, 32 (1997) 51-63.

[5] Howard S. Bender, Overview of polyurethane dispersion chemistry, FSCT Coating Fundamental: Waterborne coating technology, (2004) 41-47.

[6] Stefan Heberer, Robert Maier, Rudiger Mertsch, Gunther Michael, Markus Pridohl, Novel UV protection coatings based on nano-ZnO particles, Smart Coatings III, Berlin 2004.

[7] Shuxue Zhou, Limin Wu, Jian Sun and Weidian Shen, The change of the properties of acrylic-based polyurethane via addition of nano-silica, Progress in Organic Coatings, 45 (2002) 33-42.

[8] Junrong Zheng, Rahmi Ozisik , Richard W. Siegel, Disruption of self-assembly and altered mechanical behavior in polyurethane/zinc oxide nanocomposites, Polymer 46 (2005) 10873-10882.

[9] L.H. Yang, F.C. Liu and E.H. Han, Effects of P/B on the properties of anticorrosive coatings with different particle size, Progress in Organic Coatings, 53 (2005) 91-98.

[10] J.González-Irun Rodrigúez, P.Carreira, A.García, A.Garcia-Diez, D.Hui, R.Artiaga and L.M.Liz-Marzián, Nanofiller effect on the glass transition of a polyurethane, Journal of Thermal Analysis and Calorimetry, 87 (1) (2004) 45-47.

[11] Shuxue Zhou, Limin Wu, Jian Sun and Weidian Shen, Effect of nanosi;ica on the properties of polyester-based polyurethane, Journal of Applied Polymer Science, 88 (2003) 189-193.

[12] Mahoammad Mehdi Jalili, Siamak Moradian, Hamed Dastmalchian, Ail Karbasi, Investigating the variations in the properties of 2-pack polyurethane clear coat through separate incorporation of hydrophilic and hydrophobic nano-silica, Progress in Organic Coatins, 59 (1) (2007) 81-87.

[13] Zoran S. Petrovi, Young Jin Cho, Ivan Javni, Sergei Magonov, Natalia Yerina, Dale W. Schaefer, Jan Ilavský, Alan Waddon, Effect of silica nanoparticles on the morphology of segmented polyurethanes, Polymer , 45 (12) (2004) 4285-4295.

[14] Ray Fernando, Nanomaterial technology applications in coatings, JCT Coatings Tech, 1 (5) (2004) 32-38.

[15] Roger H. Cayton, Thomas Swaitowski, The Impact of Nano-Materials on Coating Technologies, NSTI-Nanotech 2005, www.nsti.org.ISBN 0-9767985-1-4 Vol.2, 2005.

[16] Norman S. Allen, Michele Edge, Amaya Ortega, Gonzalo Sandoval, Christopher M. Liauw, J. Verran, John Stratton and Robert B. McIntyre ,Degradation and stabilization of polymers and coatings: nano versus pigmentary titania particles, Polymer Degradation and Stability, 85 (3) (2004) 927-946.

[17] A.Ammala, A.J.Hill, P.Meakin, S.J.Pas and T.W.Turney, Degradation studies of polyolefins incorporating transparent nanoparticulate zinc oxide UV stabilizer, J.of Nanoparticle Research, 4 (2002) 167-174.

[18] Roger H.Cayton and R.W.Brotzman, Jr., Nanocomposite Coatings-Applications and Properties, Mat.Res.Soc.Symp.Proc.703 (2002) V8.1.1-V8.1.6.

[19] Lucas J. Brickweg, Bryce R.Floryancic, Erik D.Sapper, and Raymond H.Fernando, Shear-induced 1-D alignment of alumina nanoparticles in coatings, Journal of Coating Technology and Research, 4 (1) (2007) 107-110.

[20] Qi Wang, Min Yang and Yunfa Chen, Effect of nanosized iron oxide with different morphology on nanomechanical properties of nanocomposite coatings, Key Engineering Materials, Vols.336-338 (2007) 2218-2220.

[21] Abdel Salam Hamdy, Advanced nano-particles anti-corrosion ceria based sol-gel coatings for aluminium alloys, Material Letters, 60 (21-22) (2006) 2633-2637.

[22] S.Kozhukharov, G.Tsaneva, V.Kozhukhuarov, J.Gerwann, M.Schem, T.Schmidt, M.veith, Corrosion protection properties of composite hybrid coatings with involved nano-particles of zirconia and ceria, Journal of the University of Chemical Technology and Metallurgy, 43 (1) (2008) 73-80.

[23] D.R.Baer, P.E.Burrows, Anter A.El-Azab, Enhancing coating functionality using nanoscience and nanotechnology, Progress in Organic Coatings, 47 (2003) 342-355.

[24] A.Kalendova, Effects of particle sizes and shapes of zinc metal on the properties of anticorrosive coatings, Progress in Organic Coatins, 46 (2003) 324-332.

[25] Hongwei Shi, Fuchun Liu, Enhou Han and Yinghua Wei, Effect of nano pigments on the corrosion resistance of alkyd coatings, J. Mater. Sci. Technol., 23 (4) (2007) 551-558.

[26] Haifeng Lu, Bin Fei, John H. Xin, Ronghua Wang, Li Li, Fabrication of UV- blocking nanohybrid coating via miniemulsion polymerization, Journal of Colloid and Interface Science 300 (2006) 111–116.

[27] S.M. Al-Hilli and M. Willander, Optical properties of zinc oxide nano-particles embedded in dielectric medium for UV region: Numerical simulation, Journal of Nanoparticle Research, 8 (2006) 79–97.

[28] B.Pacaud, J.N.Bousseau, J.Lemaire, Nano-titania as UV blocker in stains, European coating journal, 11 (1998) 842-848.

[29] H.Kastien, Conference Proceedings Nanotechnologies in der Lackpraxis, Vincent, (2004) 21-31.

[30] Zhou, S, Wu, L, Sun, J, Shen, W, ''Effect of Nanosilica on theProperties Of Polyester-Based Polyurethane.'' J. Appl. Sci.,88 (2003) 189–193 .

[31] S.K.Dhoke, Rohit Bhandari, A.S.Khanna, Formulation of nano-ZnO incorporated silicone modified alkyd based waterborne coating and evaluation of its Mechanical and Heat resistance property, Progress in Organic Coatings, 64 (2009) 39-46.

Photocatalytic Inactivation of Bacteria by Tio_2-based Compounds under Simulated Sunlight Irradiation

Li Zhang [1, 2, 3], Jianhui Yan[1, 2], Minjie Zhou [2], Younian Liu[1]

[1] College of Chemistry and Chemical Engineering, Central South University, Changsha, China

[2] School of Chemistry and Chemical Engineering, Hunan Institute of Science and Technology, Yueyan, China

[1]lynphotocatalyst@163.com; [2]yanjh58@163.com; [3]hgx.zl@163.com

***Abstract*- $CuCr_2O_4$ nanoparticles have been successfully synthesized via a facile citric acid (CA)-assisted sol-gel method, and further combined with TiO_2 (Degussa P25) by solid phase method. These obtained photocatalysts were characterized by X-ray diffraction (XRD) and UV-vis diffuse reflectance spectrum (UV-vis DRS). Then the photocatalytic inactivation of Escherichia coli, a Gram-negative bacterium, was performed with the photocatalysts in suspension to investigate the photocatalytic bactericidal activities under simulated solar light irradiation. The results show that $CuCr_2O_4/TiO_2$ composite photocatalysts exhibited much better photocatalytic activity than either pure $CuCr_2O_4$ or TiO_2. The effects of $CuCr_2O_4$ to TiO_2 mass ratio, calcination temperature, initial concentrations of *E. coli* and concentrations of catalysts on photocatalytic bactericidal activities over the as-obtained photocatalysts were investigated in detail. The results show that when the concentration of photocatalyst is 0.5 g L^{-1}, the optimal photocatalytic sterilization rate for E. coli (10^5 CFU/mL) over $CuCr_2O_4/TiO_2$ with a 90% content of TiO_2, calcination at 500 °C reached 99.8% within about 40 min, which is 1.62 and 1.33 times more than that of $CuCr_2O_4$ and TiO_2, respectively.**

Keywords*- *Escherichia Coli; $Cucr_2O_4/Tio_2$; Photocatalytic Inactivation; Simulated Sunlight Light

I. INTRODUCTION

Since Matsunaga et al. reported for the first time that TiO_2 photocatalyst could kill bacterial cells in water [1], many research groups have reported the application of semiconductor photo-catalysis to the inactivation of different kind of pathogenic microorganisms, such as bacteria, viruses, algae, fungi or protozoa [2]. The bactericidal effects of TiO_2 photocatalysis, and especially the inactivation of E.coli suspensions, are by far, the most reported studies [3-4]. Several studies have focused on the study on the effects of operational parameters such as light intensity and titanium dioxide concentration [5-6], and the use of solar light[7]. However, TiO_2 has a large band gap(anatase, 3.2 ev; rutile, 3.0 ev), and therefore only UV light (λ<385 nm) can be absorbed, accounting for merely 5% of the sunlight energy. To solve these problems, numerous studies, including impurity doping [8-13], have been performed recently to enhance the photocatalytic efficiency and visible light utilization of TiO_2.

Recently, our group has reported that the metal ions of Cu, Co, Fe doped TiO_2 possesses high photocatalytic activity for H2 production [14-15]. We also found that $CuO/CoFe_2O_4$-TiO_2 possesses better photocatalytic bactericidal effect against E. coli than TiO_2 under simulated solar light irradiation. Because energy gap of CuO (Eg = 1.2eV) is too narrow, the valence band potential may be lower than cell oxidation potential and the narrow-band gap may be occur optical corrosion, which reduce the photocatalytic oxidation ability. The results suggest that the development of better visible light photoatalysts depends on the visible light photoresponse and highly effective interfacial charge-transfer.

In this paper, $CuCr_2O_4$ nanoparticles were synthesized via a facile CA-assisted sol-gel method and $CuCr_2O_4/TiO_2$ composite photocatalysts were prepared by solid phase method, whose photocatalytic activity based on inactivation of the bacteria Escherichia coli was investigated under simulated sunlight irradiation. The effects of several factors of composite photocatalysts on the survival ratio of E. coli were studied.

II. EXPERIMENTAL SECTION

A. Chemicals and Materials

Titania P25 (70% anatase, 30% rutile) was purchased from Degussa Co; Escherichia coli (E.coli DH-5a) was from the Microbiology Laboratory of Hunan Institute of Science and Technology. All other chemicals were of analytical grade. Deionized and doubly distilled water was used throughout this study.

B. Preparation of Photocatalysts

$CuCr_2O_4/TiO_2$ composite photocatalysts were prepared by solid phase method. Briefly, 0.005 mol $Cu(NO_3)_2$ and 0.01 mol $Cr(NO_3)_3$ were dissolved together in 50 ml distilled water to get a mixed solution. The mixed solution was subsequently added into 100 ml 0.3 M citric acid (CA) solution under stirring, and produced a transparent mixed soluble. During this mixing procedure, the temperature was controlled at around 50 ^oC by using a water bath. Then the temperature was further kept at 80 oC until a transparent and viscous gel was obtained. The as-obtained gel was subsequently transferred into an oven and kept at 130 ^oC for 3 hours. The as-prepared precursor was then annealed at certain temperature for 1.5 hour with a heating rate of 10 oC /min. $CuCr_2O_4/TiO_2$ heterojunction was synthesized via the same route by adding a certain amount of Degussa P25 TiO_2 in the raw materials preparation when the transparent mixed sol had been obtained.

C. Characterization of Photocatalysts

The crystal phase of the as-prepared photocatalysts were identified by powder X-ray diffraction method (XRD, Bruker D8) using Cu Kα radiation (λ =1.5418Å) at a scan rate of 4^oC/min. The UV-vis diffuse reflectance spectrum (UV-vis DRS) of the as-prepared photocatalysts was measured with an UV-vis spectrometer (Shimadzu UV-2500).

D. Photocatalytic Reaction Procedure

Bacteria cell was prepared according to the reference [16]. E. coli, a gram-negative bacterium, was used as model bacteria in this study. They were incubated in Luria-Bertani (LB) nutrient solution at 37 ^oC for 18 hours with shaking, and then washed by centrifugation at 4000 rpm. The treated cells

were then re-suspended and controlled from 104 to 108 colony-forming units (cfu/mL) with 0.9% saline. All materials used in the experiments were autoclaved at 121 °C for 25 min to ensure sterility. The diluted cell suspension and photocatalyst were added to a 100 mL beaker with a cover. The final photocatalyst concentration was adjusted to 0.6 g/L, and the final bacterial cell concentration was 107cfu/mL. The reaction volume was 30 mL. The reaction mixture was stirred with a magnetic stirrer throughout the experiment. The light source for photocatalysis was a xenon lamp (Model No: DX-150; wavelength, 200-900nm (unfiltered), 150W). Light was passed through without filter and then was focused onto the beaker reactor. With two air exhaust fan for thermal dissipation, the reaction temperature was maintained from room temperature to a maximum 35°C under illumination. A bacterial suspension without photocatalyst was irradiated as a control and the reaction mixture with no light irradiation was used as a dark control. At different intervals during the experiment, certain amount of the reaction solution was taken and diluted with saline and the samples with the appropriate dilution were incubated at 37°C for 18 hours on nutrient agar medium. Then the colonies were counted to determine the number of viable cells. The survival ratio of Escherichia coli was calculated by the ratio of the number of viable colonies and that of viable colonies present initially. All the above experiments were repeated three times and the average values were given.

III. RESULTS AND DISCUSSION

A. Photocatalyst Characterization

Fig. 1 shows XRD patterns of $CuCr_2O_4$/ TiO_2 calcination at different temperature. $CuCr_2O_4/TiO_2$ calcined at 500-700 had better crystallinity. The diffraction peaks of $CuCr_2O_4/TiO_2$ calcined at 300°C were flat, indicating the bad crystallinity. As the increase of calcination temperature, the diffraction peaks of anatase TiO_2 become weaker while that of rutile TiO_2 become stronger, implying the appearance of anatase-to-rutile (A-R) phase transformation. The rutile TiO_2 becomes dominant at a higher calcination temperature. It could clearly be seen that TiO_2 in the composite catalysts presented mainly in the form of rutile, when the calcination temperature is higher than 500°C. In addition to the anatase and rutile phase of TiO_2, the diffraction peaks attributed to $CuCr_2O_4$ were observed. The crystallite size of $CuCr_2O_4$ was 50 nm as calculated with the Debye-Scherrer equation from the line width of the XRD data. The diffraction peaks of $CuCr_2O_4$ become stronger with the increase of calcination temperature, revealing that the crystallinity improves.

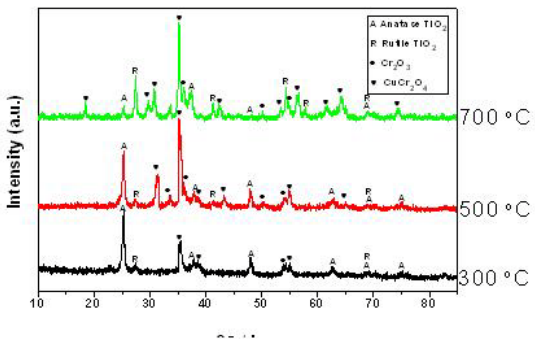

Fig. 1 XRD patterns of the $CuCr_2O_4/TiO_2$ 90% photocatalysts calcined at different temperature

The UV-vis DRS spectra of the photocatalysts is described in Fig. 2. Compared to TiO_2, both $CuCr_2O_4$ and $CuCr_2O_4/TiO_2$ composite exhibit excellent absorption ability, especially $CuCr_2O_4$, which can efficiently absorb the light ranging from UV to visible region

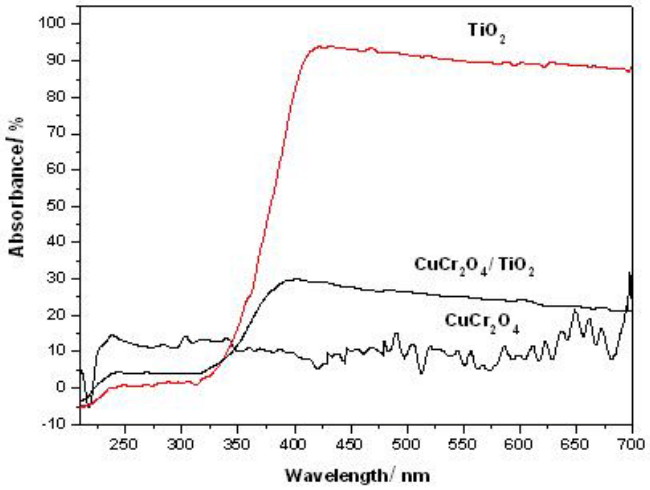

Fig. 2 UV-vis DRS spectra of the different photocatalysts

B. Effect of TiO_2 Content on E. Coli Inactivation

The photocatalytical sterilization result is presented in Fig. 3. The survival ratio of E. coli in the composite photocatalysts is related to the content of TiO_2. The sterilization activity increases linearly with the TiO_2 content until a certain value around 90%, reaching a plateau for higher values. $CuCr_2O_4/TiO_2$ 90% have displayed the maximum killing capacity in the given time and the survival ratio of Escherichia coli decreased to nearly zero in 40 min, whereas other content of TiO_2-based suspension achieved a decrease to nearly zero in 50 or 60 min.

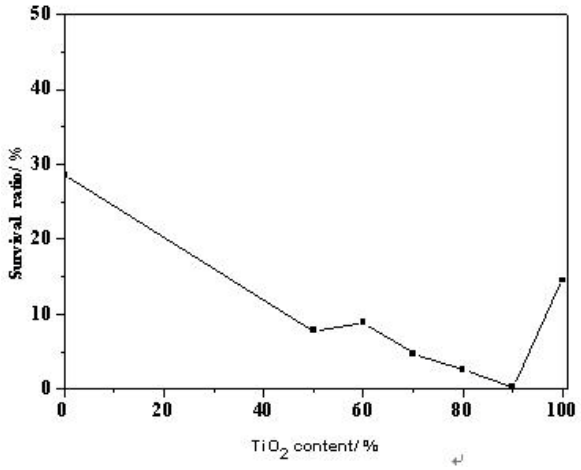

Fig. 3 Effect of different content of TiO_2 on photokilling of E. coli (reaction conditions: calcination temperature: 500°C; irradiation time: 40 min)

These results show that $CuCr_2O_4/TiO_2$ disinfection rate is faster than that of the pure TiO_2, and $CuCr_2O_4/TiO_2$ photocatalyst has promising effects on the disinfection of E. coli, as it enhanced the speed and minimised the time required for the disinfection process. This finding is of direct relevance in applications where treatment time is of importance. Although the amount of $CuCr_2O_4$ with respect to TiO_2 is very small (mass ratio of 1:9), the enhancement of photokilling rate is significant. This effect may arise from the combination of $CuCr_2O_4$ and TiO_2. An appropriate $CuCr_2O_4$ to TiO_2 mass ratio

in the composite can maximize the transfer of photogenerated electrons from $CuCr_2O_4$ to TiO_2, so as to minimise e-h recombination and increase the opportunity for oxidizing surface by positive holes to form increased concentration of hydroxyl radicals (• OH), which in turn have strong oxidative decomposing power[17]. The • OH radicals are even more oxidative thanmO_2- and can react with organic matter such as cells and E. coli to destroy them[18].

C. Effect of Calcination Temperature

Fig. 4 summarizes the survival ratio of E. coli using the $CuCr_2O_4/TiO_2$ 90% as a function of the calcination temperature. The survival ratio of E. coli decreases with the calcination temperature from 200 to 500°C, reaches its minimum at 500°C, and thereafter increases. Good crystallinity is very important to the activity of catalyst [19]. As is shown in the XRD results (Fig. 1), the $CuCr_2O_4$ shows poor crystallinity at lower calcination temperature, and the crystallinity improves as the calcination temperature increases, resulting in lower survival ratio of E. coli. The survival ratio of E. coli is only 6.8% within 30 min under the xenon lamp irradiation when the calcination temperature is 500°C. Although a higher calcination temperature can improve the crystallinity, it can also decrease the surface area of nanoparticles and cause the TiO_2 change from anatase to rutile [20]. As a result of small surface, it can absorb fewer photons and provide a longer transfer path, leading to more recombination of electron and hole, on the other hand, at higher temperature, catalyst transforms to the rutile phase that its catalytic activity is very poor[21]. Therefore, the photocatalytic inactivated rate of E. coli decreases at higher calcination temperature.

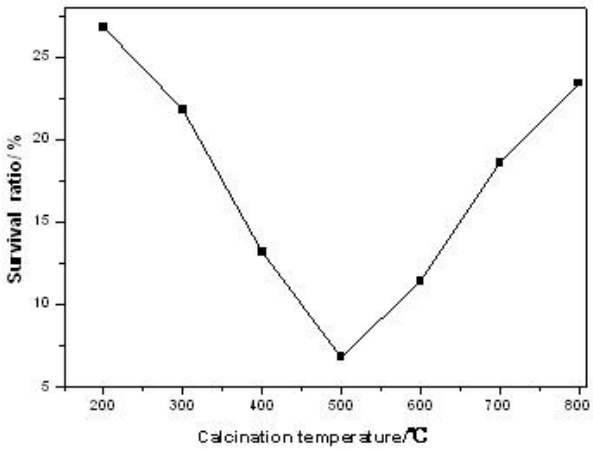

Fig. 4 Effect of the calcination temperature on the survival ratio of Escherichia coli over the as-obtained CuCr2O4/TiO2 90%

D. Effect of Different Initial Concentrations of E. Coli

The effects of different initial concentrations of E. coli (104-106 CFU/mL) on photacatalytic activity are shown in Fig. 5. From the figure, it is clear that with the increase of initial concentration of E. coli, the complete sterilization time using CuCr2O4/TiO2 90% is correspondingly increased. 104 CFU/mL and 105 CFU/mL of E. coli are completely inactivated within 40 min, and under the same conditions it takes 60 min to completely kill 106 CFU/mL of E. coli. Some reports found that the rate of bacterial inactivation in prophase was faster than that of anaphase where it needed a long time to kill the remaining cells, and the result met the first-grade kinetics rule [22].

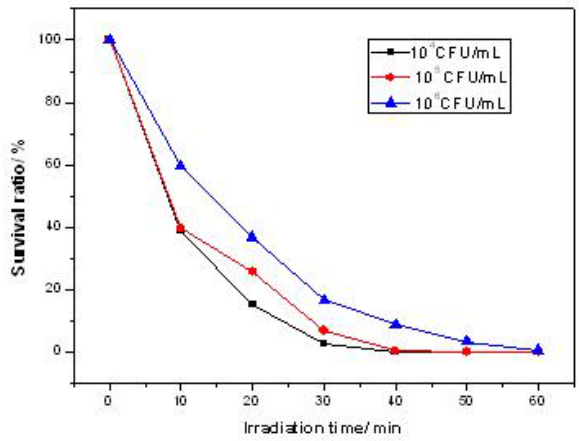

Fig. 5 Effect of different initial concentrations of E. coli on the survival ratio of Escherichia coli over the as-obtained $CuCr_2O_4/TiO_2$ 90% calcined at 500°C

E. Effect of the Photocatalyst Concentration

The photocatalytic bactericidal activities of $CuCr_2O_4/TiO_2$ 90% with different concentrations are shown in Fig. 6. The activity increases with the increase of the photocatalyst concentrations. However, the photocatalytic bactericidal rate reaches its maximum at the photocatalyst concentration of 0.5 g L−1. And Escherichia coli were almost completely inactivated within about 40 min when the initial concentration of E. coli is 105 CFU/mL. It is well known that the active centre number on catalyst particle surfaces and the penetration ability of incident light in reactor are extremely important for the photocatalytic activity [23]. Generally, larger catalyst concentration provides more catalytically active centres for the absorption of photons, and then more electrons and holes are generated. However, the excess photocatalyst may act as an optical filter and impede the further penetration of incident light into the suspension. We observed that the photocatalytic bactericidal activity increases with increasing the $CuCr_2O_4/TiO_2$ 90% concentrations when the concentration is lower than 0.5 g L−1, whereas it decreases with further increasing photocatalyst. In addition, the activated particles can be deactivated by the collision with the inactivated particles which act as electron-hole trappers, resulting in charge loss.

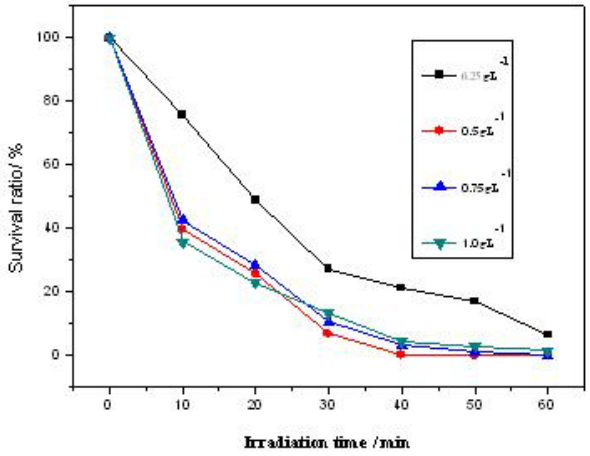

Fig. 6 Effect of the photocatalyst concentration on the survival ratio of Escherichia coli over the as-obtained $CuCr_2O_4/TiO_2$ 90% calcined at 500°C

F. Effect of Different Experimental Conditions

Fig. 7 illustrates the survival ratio of E. coli under

simulated sunlight or dark condition. The sterilization activity of $CuCr_2O_4/TiO_2$ is superior to TiO_2 or $CuCr_2O_4$ under simulated solar light irradiation. The optimal photocatalytic sterilization amount of $CuCr_2O_4/TiO_2$ is 1.62 and 1.33 times more than that of $CuCr_2O_4$ and TiO_2, respectively, which owing to the appropriate combination of $CuCr_2O_4$ and TiO_2 can help to the transfer of photogenerated electrons from $CuCr_2O_4$ to TiO_2, improving the separation of photogenerated e-h pairs, as discussed above in section 3.2. It was noted that the Pd additive can also promote visible-light absorption in nitrogen-doped TiO_2 [24]. The visible light absorption is essential to the charge production on the semiconductor photocatalyst [25]. Such dual roles of $CuCr_2O_4$ significantly enhanced the photocatalytic activity of $CuCr_2O_4/TiO_2$ under visible-light illumination.

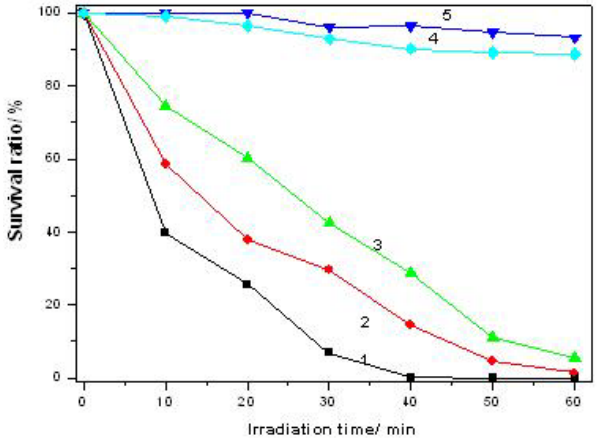

Fig. 7 Comparison of survival ratio of E.coli under different experimental conditions (reaction conditions: $mCuCr_2O_4$: $mTiO_2$=1: 9; irradiation time: 60 min): 1. E. coli + $CuCr_2O_4/TiO_2$+light; 2. E. coli +TiO_2+ light; 3. E. coli + $CuCr_2O_4$+ light; 4. Light only without catalyst; 5. E.coli + $CuCr_2O_4/TiO_2$ + dark

The result of this study also showed that there is no significance change in microbial count of the $CuCr_2O_4/TiO_2$ photocatalyst placed in the dark (Fig. 7). The survival ratio of E. coli still reaches 93.21% after 60 min irradiation. Minor variations in the bacterial count are due to experimental errors and variations arising during the sampling procedure where "true" darkness could not be ascertained. Therefore, the $CuCr_2O_4/TiO_2$ itself is nontoxic to E. coli.

Irradiation without catalyst doesn't exhibit a good effect of sterilization. After 60 min, the survival ratio of E. coli still reaches 88.72%. Comparing with dark condition, the antibacterial property under simulated sunlight condition with $CuCr_2O_4/TiO_2$ 90% has a great improvement, and the survival ratio of E. coli is only 6.8% within 30 min under the xenon lamp irradiation. Therefore, both light and catalysts play a significant role on photocatalytic inactivation of E. coli.

IV. CONCLUSIONS

$CuCr_2O_4/TiO_2$ composite photocatalysts were successfully synthesized via the facile citric acid (CA)-assisted sol-gel method and solid phase method. The as-obtained photocatalysts exhibits higher photocatalytic sterilization activity compared with pure $CuCr_2O_4$ or TiO_2 for killing Escheri chia coli under the xenon lamp of 150W irradiation. When the concentration of photocatalyst is 0.5 g L^{-1}, the optimal photocatalytic sterilization rate for E. coli (105 CFU/mL) over $CuCr_2O_4/TiO_2$ 90%, calcination at 500C can be achieved, 99.8% Escherichia coli can be sterilized within 40 min under simulated sunlight irradiation.

ACKNOWLEDGEMENTS

This project was financially supported by the National Nature Science Foundation of China (No.20876039), Scientific Research Fund of Hunan Provincial Education Department (No.10B042), and Aid Program for Science and Technology Innovative Research Team in Higher Educational Institutions of Hunan Province.

REFERENCES

[1] T. Matsunaga, R.Tomoda, T. Nakajima, H. Wake, FEMS Microbiol. Lett. 29 (1985) 211-214.

[2] C. McCullagh, J. M. C. Robertson, D. W. Bahnemann, P. K. J. Robertson, Res. Chem. Intermed. 33 (2007) 359-375.

[3] P. S. M. Dunlop, J. A. Byrne, N. Manga, B. R. Eggins, J. Photochem.Photobiol. A: Chem. 148 (2002) 355-363.

[4] H. M. Coleman, C. P. Marquis, J. A. Scott, C. C. Chin, R. Amal, Chem. Eng. J. 113 (2005) 55-63.

[5] Y. Horie, D. A. David, M. Taya, S. Tone, Ind. Eng. Chem. Res. 35 (1996) 3920-3926.

[6] A. K. Benabbou, Z. Derriche, C. Felix, P. Lejeune, C. Guillard, Appl. Catal. B-Environ. 76 (2007) 257-263.

[7] P. Ferna ′ndez, J. Blanco, C. Sichel, S. Malato, Catal. Today. 101 (2005) 345-352.

[8] S. Takashi, T. Masahito, Biochem. Eng. J. 30 (2006) 199-204.

[9] L. Li, M. Lei, T. Sakae, Mater. Sci. Eng., B. 148 (2008) 183-186.

[10] S. Funda, A. Meltem, K. Nadir, J. Hazard. Mater. 162 (2009) 1309-1316.

[11] H. Irie, Y. Watanabe, K. Hashimoto, Chem. Lett. 32 (2003) 772-773.

[12] D. M. Chen, D. Yang, Q. Wang, Z. Y. Jiang, Ind. Eng. Chem. Res. 45(2006) 4110-4116.

[13] V. Subramanian, E. E. Wolf, P. Kamat, J. Am. Chem. Soc. 126(2004) 4943-4950.

[14] Yang, H. H.; Yan, J. H.; Lu, Z.G. *J.* Alloys. Compd. 476(2009) 715-719.

[15] Yan, J. H.; Yang, H. H.; Tang, Y. G. *Renew Energy*. 34(2009) 2399-2405.

[16] Y. Q. Lan, C. Hu, X. X. Hu, Appl. Catal. B-Environ. 73(2007) 354-360.

[17] A. Vohra, D.Y. Goswami, D. A. Deshpande, S. S. Block, J Ind Microbiol Biotechnol. 32 (2005) 364-370.

[18] R. Vasant Kumar, R. Ghulam, Ionics. 15 (2009) 579-587.

[19] S. T. Valdes, G. Marban, A. B. Fuertes, Catal. Today. 116 (2006)354-360.

[20] T. Tsumura, N. Kojitani, I. Izumi, N. Iwashita, M. Toyoda, M. Inagaki, J. Mater. Chem. 12 (2002) 1391-1396.

[21] M. Hamadanian, A. Reisi-Vanani, A. Majedi, Appl. Surf. Sci. 256(2010) 1837-1844.

[22] Rincon, A. G.; Pulgarin, C. *Appl. Cata. B: Environmental.* 2004, 44, 263.

[23] S. Ullah, A. H. Dogar, N. Mehmood N, Ion-induced secondary electron emission from MgO and Y_2O_3 thin films, Vacuum 84 (2010) 509-513.

[24] Q. Li, R. Xie, E. A. Mintz, J. K. Shang, J. Am. Ceram. Soc. 90 (2007) 3863-3868.

[25] P.G. Wu, R. C. Xie , J. A. Imlay, J. K. Shang, Appl. Catal. B-Environ. 88 (2009) 576-581.

Modeling of Radar Absorbing Materials Using Winning Particle Optimization Applied on Electrically Conductive Nanostructured Composite Material

Davide Micheli, Roberto Pastore, Mario Marchetti

Department of Astronautic, Electric and Energy, Sapienza University of Rome
Roma, Italy
davide.micheli@uniroma1.it; roberto.past@gmail.com; mario.marchetti@uniroma1.it

Abstract- **Modelling and manufacturing of radar absorbing material are proposed using multilayer composite nanostructured materials and the recently introduced winning particle optimization algorithm. The study concerns tile of materials with dimensions of 0.3m×0.3m made of nanostructured composite materials, which consist on epoxy-resin and industrial grade carbon nanotube (CNTs) fillers. The industrial grade CNTs were appositely chosen for their low costs, in order to be applied in great amount to build large tile of composite materials. Here modelling takes into account for an extended frequency band (5 to 18 GHz), for several incidence angles of the electromagnetic field (0 to 80°), and for the minimization of the electromagnetic reflection coefficient. At last simulations are compared with measurements of reflection coefficient. Despite some errors mostly due to the manufacturing process, simulations are in good agreement with measurements, showing an interesting approach to design multilayer radar absorbing materials.**

Keywords- Radar Absorbing Materials; Evolutionary Computation; Winning Particle Optimization; Modeling; Carbon Nanotubes; Composite Nanostrucutred Materials; Layered Structures; Non-Destructive Testing; NRL-Arch; Stealth

I. INTRODUCTION

Radar absorbing materials (RAM) acquired importance since their first applications in military field [1-6]. Germany pioneered the first aircraft to use RAM during World War II, in the form of the "Horten Ho 229", in order to reduce the radar signature, and concerned with radar camouflage for submarines, developed "Wesch" material, a carbonyl iron powder loaded rubber sheet about 0.3 inches thick and a resonant frequency at 3 GHz. Composite materials considered in this work are based on epoxy matrix reinforced with carbon nanomaterials. These latter were chosen taking into account their good microwave absorption behaviour [7] and the low market prices. In fact, the economic aspects, normally neglected in small laboratory applications, are important in real applications where the amount of carbon nanopowders fillers could be relatively high. In such scenario, a good compromise in terms of cost/performances was obtained using industrial grade multiwall carbon nanotubes (MWCNTs) with a cost of about 300 $/kg. MWCNTs with commercial name of NANOCYLTM NC7000 (diameter around 9.5 nm, length 1.5 μm, purity 90%) were bought at NANOCYL. Bi-component Epoxy-resin PrimeTM 20LV (density 1.123 g/cm^3) with Hardner (density 0.936 g/cm^3) was used as matrix. RAM is based on layered materials where each layer is made of carbon nanostructured composites materials in different weight percentages. The recent developed winning particle optimization search algorithm (WPO) was applied in order to design and optimize multilayer materials able to effectively absorb microwaves in the range 5 GHz to 18 GHz. The paper is organized in 5 distinct sections. In Section II, mathematical model of absorber is shown; in Section III, WPO is described; in Section IV, numerical design of RAM is discussed and in Section V, RAM manufacturing and electromagnetic performance comparisons between simulation and manufactured RAM are shown. In this section the adopted experimental setup is accurately described showing the NRL-arch test fixture. It is crucial to highlight the interdisciplinary research activity through nanomaterials, electromagnetic wave propagation theory, composite materials manufacturing techniques and search computation algorithms. All of them are required to design the "quasi perfect absorber".

II. RAM MATHEMATICAL MODEL

WPO algorithm [8-9], has been applied to solve a quite complex problem consisting in the design and optimization of microwave absorbing multilayer materials.

Optimized RAM is based on nanomaterials in particular carbon nanostructured composites materials. Conductive fillers have been uniformly dispersed in an epoxy resin at different weight percentages (0.5, 1, 2, 2.5, 3 wt %). In Table I, six different composite materials and the index code adopted by WPO to identify each material are shown.

TABLE I
CODING OF MATERIALS IN THE DATA BASE

Materials	Materials Code
Epoxy- Resin	1
MWCNT, 0.5 wt%	2
MWCNT, 1.0 wt%	3
MWCNT, 2.0 wt%	4
MWCNT, 2.5 wt%	5
MWCNT, 3.0 wt%	6

The resulting composites samples have been dielectrically characterized in a previous work [10-11] by waveguide measurements to recover the dielectric properties of the composite materials in the data base (DB). In this paper the DB of these dielectric parameters as function of frequency is used to supply the WPO modeling algorithm. In Table II, a brief summary of the dielectric permittivity of composite materials at 6GHz, 12 GHz, 18 GHz, is shown. After that, numerical simulations of RAM have been carried out. In particular, electromagnetic analysis has been performed integrating the

forward/backward propagation formalism to the *in-house* built WPO, thus able to carry out optimization upon oblique incidence angles over a finite angular range.

TABLE II DIELECTRIC PERMITTIVITY OF COMPOSITE NANOSTRUCTURED MATERIALS

Materials	**Real Part and Imaginary Part**					
	F1= 6 Ghz		***F2= 12 Ghz***		***F3=18 Ghz***	
Epoxy- Resin	3.11	0.10	3.07	0.08	3.07	0.08
MWCNT, 0.5 Wt%	5.52;	0.90	5.33	1.81	5.21	2.83
MWCNT, 1.0 Wt%	9.52	5.27	6.75	2.88	5.39	1.95
MWCNT, 2.0 Wt%	11.42	6.89	8.82	4.48	7.45	3.38
MWCNT, 2.5 Wt%	12.90	11.28	10.86	10.35	9.71	9.79
MWCNT, 3.0 Wt%	18.21	14.50	17.29	13.65	16.72	13.31

The developed code minimizes reflection and transmission coefficients under the thickness minimization constraint. Finally, *broadband quasi-perfect absorbers* in the band 5-18 GHz are achieved combining the filler families, i.e., exhibiting a loss factor (*LF%*) greater than 90% in most of the band, for thicknesses ranging between 5 and 12 mm. Main goal of design and optimization work was to achieve values (< -10 dB) of reflection coefficients (*RC*), for angular apertures within 40° in the most part of the frequency band. The design/optimization is basically a *minimization* procedure which seeks the best trade-off between structure thickness (to be minimized) and absorbed EM power (to be maximized). The absorbing power has been quantified through the so-called "loss factor" *LF%*, defined as follows [10-11].

$$LF\% = \left(1 - |RC|^2 - |TC|^2\right)\cdot 100. \qquad (1)$$

In RAM systems the transmission coefficient *TC=0* (because of the perfect electric conductor (PEC) layer at the end of the multilayer), and the *RC* is the WPO-optimized reflection coefficient.

Both are expressed in the linear form. LF% physical meaning is related to the fraction of the incident power vanishing inside the materials because of localization and dissipation phenomena. Since the calculation of *RC* becomes a crucial point for RAM optimization goal, a rigorous approach for computing reflected waves at each layer has been adopted [11-13].

Both normal and oblique incidences have been evaluated during the automatic optimization. In Fig. 1, a general scheme of the electromagnetic absorbing multilayer structure is presented. Each layer is generally denoted by index *x*.

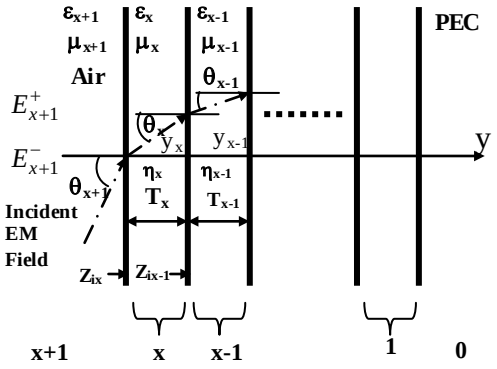

Fig. 1 General Multilayer scheme of electromagnetic absorbing structure; in RAM systems the back layer is a perfect electric conductor (PEC).

As far as geometric properties of multilayer structures are concerned, thickness of each layer can range from 0 to 10 mm, while the number of layers is upper-bounded to *maximum* 10 layers. The effective number of layers is established by the WPO optimization procedure which is able to remove one or more useless layers from the multilayer structure. The order of layer materials is not *a priori* fixed; instead WPO algorithm decides which material need to be used for each layer.

In RAM applications, *RC* at the air-absorber interface can be evaluated by the following equation relating the free space impedance to the input impedance seen at the air-multilayer structure interface

$$RC^{TM/TE} = \frac{Z_i^{TM/TE} - Z_0^{TM/TE}}{Z_i^{TM/TE} + Z_0^{TM/TE}}, \qquad RC_{dB}^{TM/TE} = 20Log_{10}\left|\frac{Z_i^{TM/TE} - Z_0^{TM/TE}}{Z_i^{TM/TE} + Z_0^{TM/TE}}\right| \qquad (3)$$

where $Z_0 \cong 377\ \Omega$ is the free space impedance and Zi is the input impedance at the first air-absorber interface. The input wave impedance of the multilayer, backed by PEC, can be expressed iterating the following equation for x-th-layer [11-13].

$$Z_{ix}^{TM/TE} = \eta_x^{TM/TE}\frac{Z_{ix-1}^{TM/TE}\cos(k_x t_x) + j\eta_x^{TM/TE}\sin(k_x t_x)}{\eta_x^{TM/TE}\cos(k_x t_x) + jZ_{ix-1}^{TM/TE}\sin(k_x t_x)} \qquad (4)$$

In (4), $t_x = y_{x-1} - y_x$ is the x-th layer thickness expressed in m, whereas the wave number k_x of each layer along y axes is

$$k_x^2 = (2\pi f)^2\mu_0\varepsilon_0\mu_{rx}\varepsilon_{rx}\cos^2\vartheta_x = (2\pi f)^2\mu_0\varepsilon_0\mu_{rx}\left(\varepsilon_{rx}^{'} - j\varepsilon_{rx}^{''}\right)\cos^2\vartheta_x \qquad (5)$$

where f is frequency of the incident electromagnetic wave in Hz, ε' is the real part of x-th-layer permittivity and ε" is the imaginary part of layer permittivity.

Complex waves appear in oblique incidence and lossy dielectrics problems [13]. Because of the wave number become complex-valued, e.g., $\vec{k} = \vec{\beta} - j\vec{\alpha}$, the angle of refraction and possibly the angle of incidence may become complex-valued too. In calculating k_x by taking square root of (5), it is required, in complex-wave problems, to get the correct signs of their imaginary parts, such that evanescent waves are described correctly. This leads to define an "evanescent" square root as follows. Let $\varepsilon_{rx} = \left(\varepsilon_{rx}^{'} - j\varepsilon_{rx}^{''}\right)$ with $\varepsilon_{rx}^{''} > 0$ for an absorbing medium, then

$$k_x^2 = \begin{cases} \sqrt{(2\pi f)^2\mu_0\varepsilon_0\mu_{rx}\left(\varepsilon_{rx}^{'} - j\varepsilon_{rx}^{''}\right)\cos^2\vartheta_x}, & \text{if } \varepsilon_{rx}^{''} > 0 \\ -j\sqrt{-(2\pi f)^2\mu_0\varepsilon_0\mu_{rx}\left(\varepsilon_{rx}^{'}\right)\cos^2\vartheta_x}, & \text{if } \varepsilon_{rx}^{''} = 0 \end{cases} \qquad (6)$$

Since all nanostructured composite materials available in the DB are with $\varepsilon_{rx}^{''} > 0$ then k_x is as usually computed.

III. WINNING PARTICLE OPTIMIZATION

WPO is a simple algorithm where at each time epoch of evolution, the particle, which best fit the objective function, is deputed to pilot the trajectory of the remaining particles within the multidimensional space of solutions, i.e., variables to be optimized. In Fig. 2, WPO flow chart is shown. At the

beginning of the iterations, particles are randomly distributed within the *n*-dimensional search space.

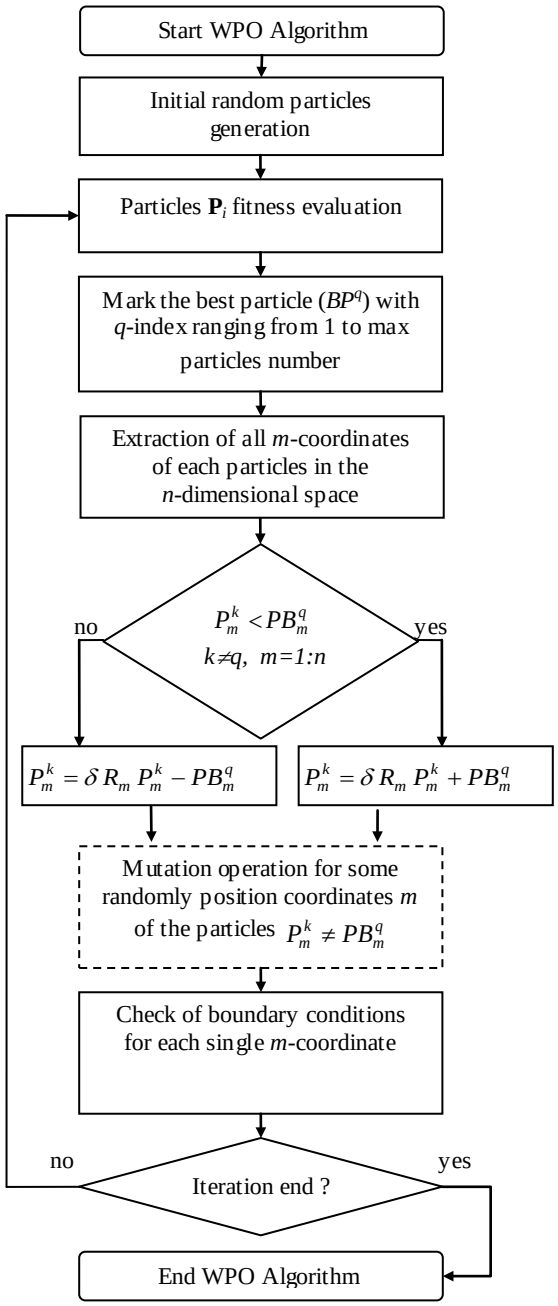

Fig. 2 WPO flow chart

At each iteration time, the objective function of each particle is computed. Then, particles are compared to each other using value of their objective function and the best fitting particle is marked with its proper index. Each particle position is completely defined by its coordinates and their number represents the dimension of the space where all particles jump searching for the optimal solution. Trajectory of each particle, except that of the best fitting particle, is defined in the following way: if *m*th-coordinate of a certain particle P^k is lesser then the corresponding *m*th-coordinate of the current best particle PB^q , then the new *m*th-coordinate will result from the sum of current particle and best particle *m*th-coordinates; while if *m*th-coordinate of a certain particle P^k is greater than the corresponding *m*th-coordinate of the current best particle PB^q, then the new *m*th-coordinate will result from the difference between the current particle *m*th-coordinates and the best particle *m*th-coordinates. Here, *q* is the index of the best particle found in each iteration and the condition which needs to be grant is $q \neq k$, i.e., all *k*th particles can be displaced except the best *q*th particle. Equation (7) describes the mentioned approach. Particle position at the *(i+1)*th iteration as a function of particle position in the previous *i*th iteration is.

$$P_m^k(i+1) = \delta R_m P_m^k(i) + g PB_m^q(i) \tag{7}$$

where

$g = +1$ if $P_m^k(i) < PB_m^q(i)$

$g = -1$ if $P_m^k(i) > PB_m^q(i)$

k = Particle index in the range [1, Particle Number]

q = Best Particle index in the range [1, Particle Number] and $k \neq q$

m = ranges in $[1, n]$

n = Space Dimensions

R_m = random number in the interval $[0, 1]$

δ = Convergence Parameter

i = current iteration in the range [1, N]

N = Number of iteration

R_m is used to randomly define the amount of displacement of each single coordinate. Such randomization develops the searching ability by conferring some causality to the amplitude of jumps. Convergence parameter δ helps the final convergence of the WPO algorithm as follows. At the beginning of the iterations, the WPO must be capable to explore the largest space of solutions as possible. On the other hand, close to the end of the iterations, high amplitude of jumps could represent a drawback since a position representing the optimal solution could forbid. In order to improve the WPO convergence, a mechanism providing a progressive reduction of "maximum jumps amplitude" has been introduced and it is identified by the δ parameter. Calling N the total number of iterations and supposing ith the current iteration, then the value of δ is given by

$$\delta = \sigma\left(1 - \frac{i}{N+1}\right)^S \tag{8}$$

$$\sigma = J(R_m - 0.5) \tag{9}$$

where *J* is the "jump amplitude" defined by the user as a numerical parameter in the main program of WPO, in this scenario it has been valued to 3 after several trials to assure a good performance in domain solution exploration.

In (8), the meaning of σ and *S* parameters is in fast or slow convergence of the WPO algorithm. In particular, the higher the σ, the greater the initial jumps amplitude and the greater the distances where particles will start to explore the search space. As far as *S* is concerned the higher its value, the faster the convergence to a suboptimal solution. The parameter σ is made using *J* and R_m such that (R_m - 0.5) is a random number between [−1/2, +1/2]. The random part of σ develops the search capability of the algorithm. Even though mutation operation has not been applied on the subsequent reported optimizations (mutation=0%), it has to be noticed that mutation can be included in WPO algorithm to further increase the random search capability. At the end of each WPO iteration, checking of boundary conditions for the new set of particles coordinates

is computed in order to avoid overcoming the constraints. The entire loop cycle can be iterated several times in order to get the required objective function minimization.

IV. RAM DESIGN AND OPTIMIZATION

The presented modeling procedure, takes into account for several incidence angles and, the design/optimization procedure can be forced to run for a one particular incidence angle or for a range of angular incidences where the global objective function has to be optimized. In particular the incidence angles here range between 0° and 80° with step 10°. As far as layer materials are concerned each one can be chosen among all of different manufactured composite materials. In Table I, all the composite materials available in the DB are reported and each composite material has been coded using an integer number.

WPO can access to DB in order to allocate the most appropriate materials for each layer of the multilayer RAM. In WPO procedures the modeling functions are called by the main program to compute: materials intrinsic impedances, in-outgoing refraction angle, TE/TM layer wave impedance, reflection coefficient (RC), and the loss factor (LF). The multilayer absorbing structures considered in the design procedure can have up to 10 layers so dimensionality of layer space is 10 i.e., $m = 10, 9 \ldots 1$.

Since the optimization are for both: layer thickness and layer material type then WPO algorithms need to be structured in order to take into account for both quantities.

In WPO algorithm we have: $T^k(i) = \left[t_{10}^k(i), t_9^k(i), \ldots\ldots, t_1^k(i)\right]$, as array of thicknesses, where $T_m^k(i)$ is the thickness of *m*-th layer, and $P^k(i) = \left[p_{10}^k(i), p_9^k(i), \ldots\ldots, p_1^k(i)\right]$, as array of material type, where $P_m^k(i)$ is the type of material associated to the *m*th layer.

The equations related to layer thicknesses and layer material for each single particle are simply updated according to,

$$\begin{aligned} T_m^k(i+1) &= \delta R_{m1} T_m^k(i) + g_{Thickness} TB_m^q(i) \\ P_m^k(i+1) &= round\left(\delta R_{m2} P_m^k(i) + g_{Material} PB_m^q(i)\right) \end{aligned} \quad (10)$$

Where, $\boldsymbol{R_{m1}}$ and $\boldsymbol{R_{m2}}$ are random numbers in the closed range 0-1, $T_m^k(i)$ is the current *k*th-particle, *m*th-layer-thickness at the *i*th-iteration, while $P_m^k(i)$ is the current *k*th-particle, *m*th-layer-material at the *i*th-iteration.

Rounded values in material equation are required since the index of material of each layer must be an integer number ranging from 1 to the number of materials available in the DB of materials.

$$\begin{aligned} g_{Thickness} &= +1 \quad \text{if} \quad T_m^k(i) < TB_m^q(i) \\ g_{Thickness} &= -1 \quad \text{if} \quad T_m^k(i) > TB_m^q(i) \\ g_{Material} &= +1 \quad \text{if} \quad P_m^k(i) < PB_m^q(i) \\ g_{Material} &= -1 \quad \text{if} \quad P_m^k(i) > PB_m^q(i) \end{aligned} \quad (11)$$

where *q* is the index of best particles *TB* and *PB*; *k* is the index of particles with $k \neq q$; *n* is the dimension number; *m* is the current dimension ranging between [1,*n*]. In the presented implementation, the value of convergence parameter *S* is set to 1.

WPO try to minimize a global objective function (*GOF*) which in turn is built using elementary objective functions (*EOF*). The *EOF* for TM and TE modes are named as $CostRC_{TM}$, $CostRC_{TE}$, for reflection coefficient. The formal definition of the *EOF* for TM and TE modes are shown in (12),(13),(14). We can observe that for each particle (*Pa*), the corresponding *EOF* is evaluated over the entire frequency band and over the entire incidence angular range, adopting frequency and angular steps chosen by the user before starting the WPO,

$$\begin{aligned} CostRC_{TM}(Pa) &= \left[\sum_{freq=f\,\min}^{freq=f\,\max}\left(\sum_{\vartheta=\vartheta\,\min}^{\vartheta=\vartheta\,\max} RC_{TM}(Pa, freq, \vartheta)\right)\right] \\ CostRC_{TE}(Pa) &= \left[\sum_{freq=f\,\min}^{freq=f\,\max}\left(\sum_{\vartheta=\vartheta\,\min}^{\vartheta=\vartheta\,\max} RC_{TE}(Pa, freq, \vartheta)\right)\right] \end{aligned} \quad (12)$$

where *Pa* is the current particle, *freq* is the frequency step, *fmin* and *fmax* is the frequency band start and stop, θ is the current angular step, θ_{min} and θ_{max} represent the angular range bounds. The definition of the EOF for thickness is

$$CostT(Pa) = \left[t_{10}(Pa) + t_9(Pa) + \ldots. + t_1(Pa)\right] \quad (13)$$

where t_m is the thickness of the *m*-th layer.

A weighting factor called α ranging in $(0<\alpha<1)$, weight CostT w.r.t. CostRC. Such weighting factor is chosen by the user and its meaning have to be intended as the capability of the tool to design the multilayer structure making privilege to the electromagnetic performances w.r.t. the thickness when α is close to 1. Final GOF is a linear combination of the described EOFs,

$$GOF(Pa) = \alpha OF1(Pa) + (1-\alpha) OF2(Pa) \quad (14)$$

where

$$\begin{aligned} OF1(Pa) &= \left(\frac{CostRC_{TM}(Pa)}{A} + \frac{CostRC_{TE}(Pa)}{A}\right) \\ OF2(Pa) &= \left[\frac{CostT(Pa)}{B}\right] \end{aligned}$$

A and B are normalization factors: A is the product between the frequency step number and the angle step number, whereas B is the product between the maximum layer number and the maximum layer thickness. In the following subsection two RAM models are shown.

A. RAM First Simulation

In the first RAM simulation a weighting factor $\alpha=0.9$ returned the scheme of layered material shown in Fig. 3.

The electromagnetic wave impinges upon the first layer made of epoxy-resin. Incidence and reflection angle is called θ^0, ranging from 0° to 80°. Total thickness of multilayer RAM is 11.77 mm and the final number of layers is 4. Tile is composed on the top by the lowest lossy material (epoxy-resin) as the first layer up to the highest lossy material in the DB (MWCNTs 3 wt%) as third layer backed by PEC. This structure can be viewed as a graded lossy system in the first three layers and a resonant structure in the fourth layer, where the chosen materials are not the highest lossy materials (MWCNTs 0.5% wt). In particular graded lossy systems are composed by a quasi-wave impedance matched material where the first interface between free space and epoxy-resin is the best coupling material able to assure the lowest reflection

coefficient at the first air-absorber interface. MWCNTs 1wt% and MWCNTs 3wt% instead have lower characteristic wave impedances and greater losses with respect to epoxy-resin and as a consequence they are placed in sequence in the layers order.

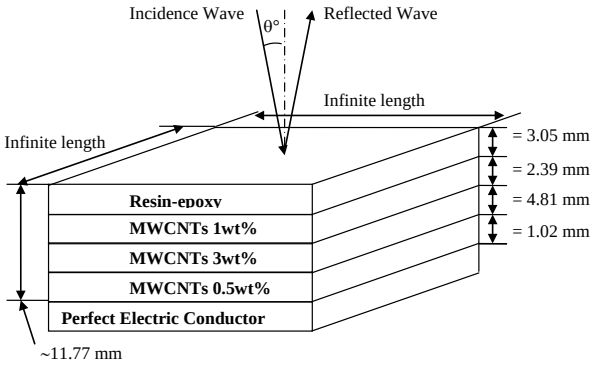

Fig. 3 RAM multilayer simulated: Resin-epoxy, MWCNTs 1wt%, MWCNTs 3wt%, MWCNTs 0.5 wt%, PEC

In Fig. 4, reflection coefficients TE/TM (dB) are shown. It can be noticed that for normal incidence angles, TE and TM curves coincides whereas around 7, 9, 12, 15 GHz, there are some incidence angles where curves show values of reflection coefficient TM even lower with respect to that at normal incidence. Such angles are denoted as Zenneck angles for lossy materials.

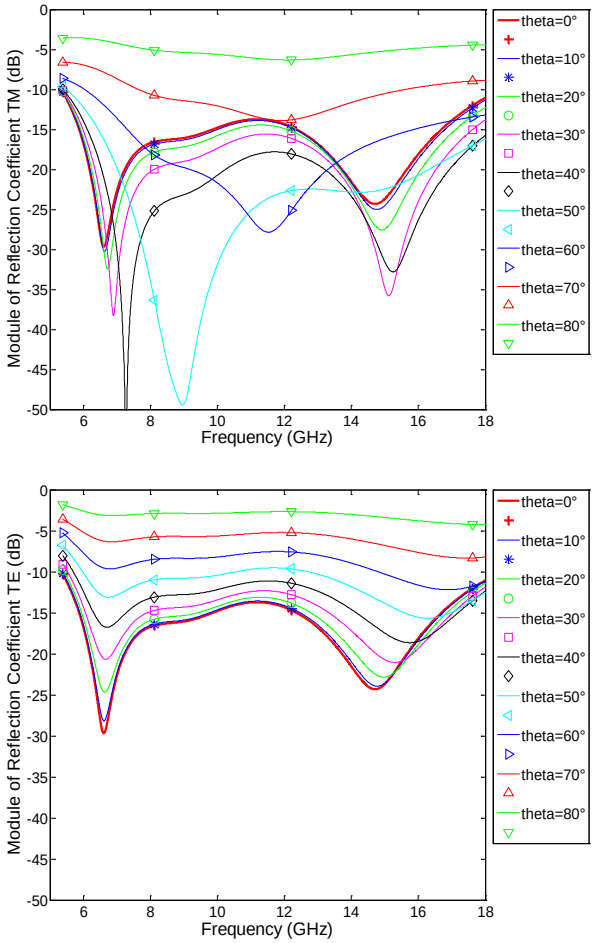

Fig. 4 RAM Reflection Coefficient (dB) TE and TM

The electromagnetic absorbing capability of a certain material is mainly due to two simultaneous conditions: "dielectric losses" within the composite material and "impedance matching condition" which in turns is a function of thickness of the absorbing layer. The impedance matching condition takes place when the electromagnetic wave impedance at the first interface between air and RAM is close to that of free space i.e., about 377 Ω. This is why in the simulation the first layer is logically made of epoxy-resin which possesses the lowest electric permittivity and so the higher electromagnetic wave impedance. The electromagnetic wave impedance at the first interface is computed using (4) and depends on dielectric parameter of all materials in the multilayer. The dielectric losses are described by the imaginary part of the permittivity (ε") while, thickness of the material is connected to the microwave wavelength within the material. The higher the dielectric losses, the greater are the electromagnetic power dissipation phenomena in the RAM composite material. Unfortunately, usually, the higher the dielectric permittivity, the lower is the electromagnetic wave impedance, which in turn mismatch the impedance matching condition with free space [11]. This is why, the RAM is composed of different layers able to progressively match the wave impedance while simultaneously assuring the right dissipation and absorbing behaviour. In Fig. 5, Loss Factor TE/TM is shown. Loss Factor (%) remains above 90% for incidence angles up to 40°. Such values mean that RAM is able to absorb the most part of the electromagnetic field reflecting back only a very little amount of the incoming energy. The extended frequency band 6 to 18 GHz where loss factor is greater than 95%, shows the interesting theoretical performance of this RAM.

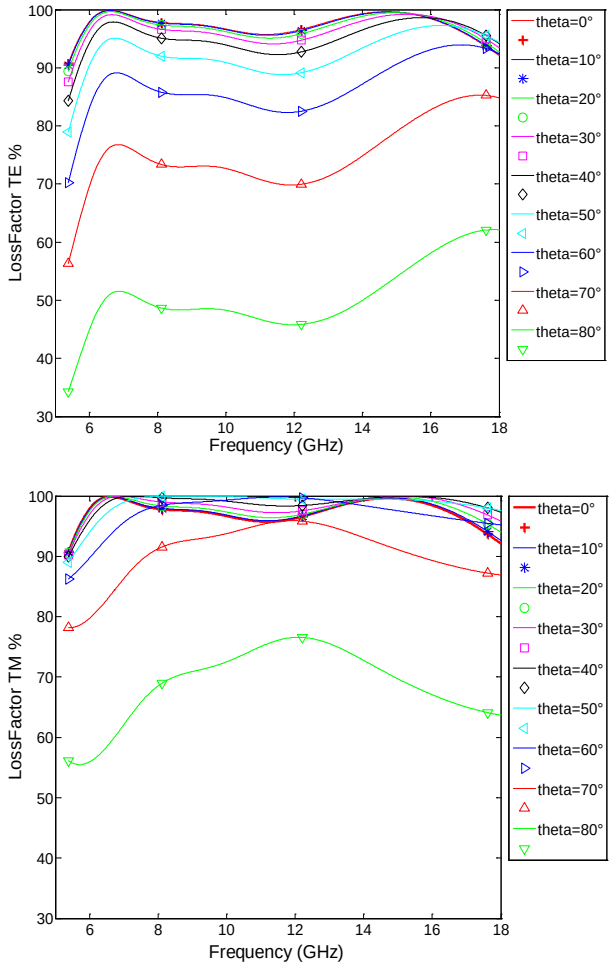

Fig. 5 RAM Loss Factor (%) TE and TM

In Fig. 6, the asymptotic convergence of WPO evolution is shown. Plot of GOF is shown. The simulation is made on 800 iterations and 256 searching particles. The time required to complete the computation strongly depends on the amount of particles and iterations and by the computer performances in terms of random memory allocation and processing speed. After 600 iterations the behaviour of curve is almost asymptotic showing a probably sufficient convergence of the WPO algorithm in searching the best solution to the RAM design and optimization problem. The computing time also depends on the way in which code is written. Here Matlab has been used. Some procedures were parallelized but others require nested loops of cycle to take into account for particles, frequencies, and incidence angles. These are very time consuming.

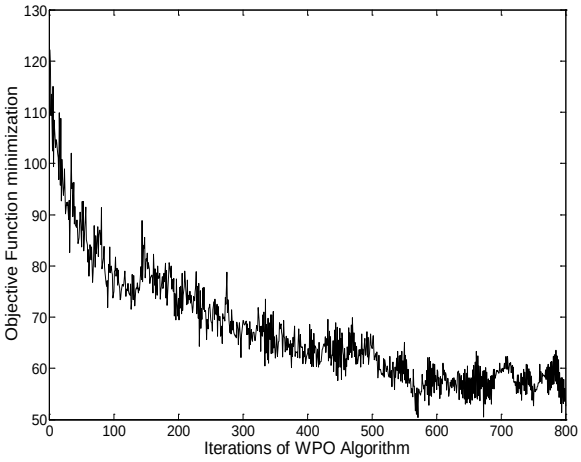

Fig. 6 WPO evolution and convergence

B. *RAM Second Simulation*

In the second RAM simulation, a lower weighting factor α=0.6 returned the scheme of layered materials shown in Fig. 7. The multilayer RAM is composed of three different layers, the first one, where the electromagnetic wave arrives, is epoxy-resin; the second one is made of MWCNTs at 1wt%, the third layer is made of MWCNTs at 2wt%. The total thickness is about 5.72 mm. In Figs. 8 and 9 the electromagnetic performances of RAM are shown.

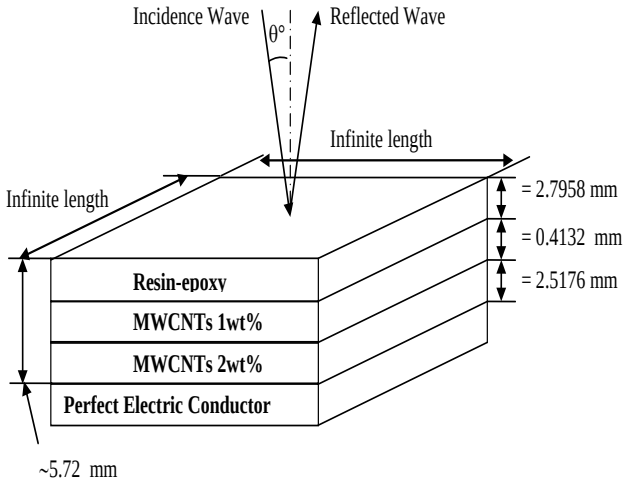

Fig. 7 RAM multilayer simulated: Resin-epoxy MWCNTs 1 wt%, MWCNTs 2wt%, PEC

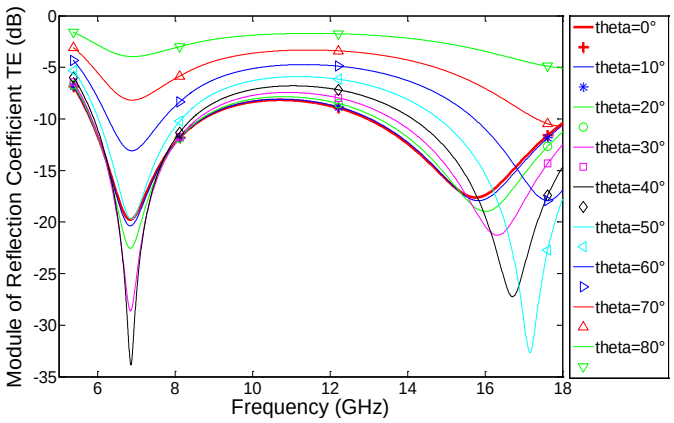

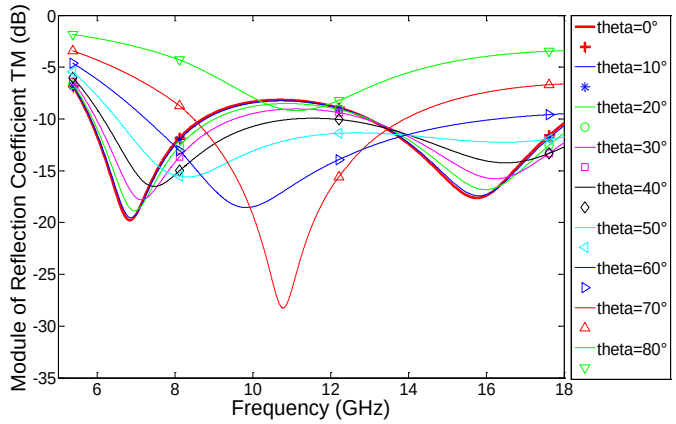

Fig. 8 RAM Reflection Coefficient (dB) TE and TM

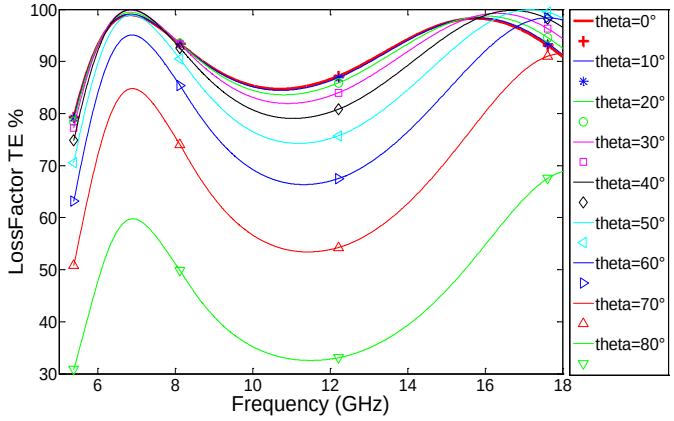

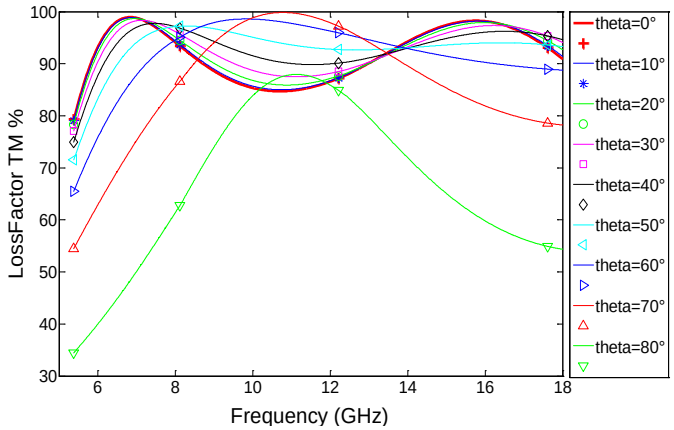

Fig. 9 RAM Loss Factor % TE and TM

The graphs show two peaks of absorption at 0° incidence angle for TE/TM around 7 and 16 GHz. When the incidence angle grows to 50°, 60° and 70° in the TM incidence mode, the first absorption packs shift to 8, 10 and 11 GHz while the second peak disappear.

V. RAM MANUFACTURING AND ELECTROMAGNETIC PERFORMANCE MEASUREMENT

The second simulated RAM multilayer scheme has been chosen as the model to try of building a large RAM tile. Each layer was manufactured over the previous using the sample holder as shown in Fig. 10. The manufacturing procedure is available in [9]. In Fig. 11, the manufactured RAM tile is shown.

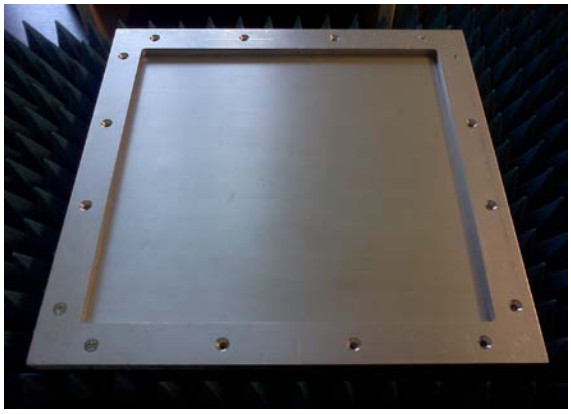

Fig. 10 Sample holder to build multilayer RAM

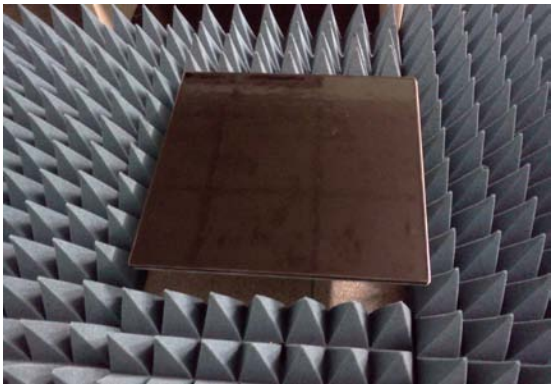

Fig. 11 Final manufactured RAM multilayer tile

The practical realization of the large RAM tile was not easy since the dimensions 30x30 cm required a lot of nanomaterials and the related dispersion process in the epoxy-resin resulted hard. Another very difficult task was to respect the thickness of each layer because the manually homemade deposition of each layer above the other one caused errors in the value of thickness and in the homogeneity of layers along the surface. The great manufacturing problems rose with the layer made of MWCNTs at 2wt%. In fact, such composite doesn't remain enough viscous so tile manufacturing process is quite difficult, especially for respect thickness constraints. At the end, the final manufactured multilayer RAM is lightly different with respect to the initial simulation reported in Fig. 7. In Fig. 12 the manufactured RAM multilayer tile scheme is shown. The total thickness of tile is about 6.1 mm. The simulation of such new tile is shown in Fig. 13. Observing the simulation it can be highlighted that even small variations of thickness layers are able to affect the reflection coefficient lowering the absorption properties of RAM. This is why it is very important to try to respect as much as possible the RAM scheme and thickness performed by WPO simulation, in the case of Fig. 7.

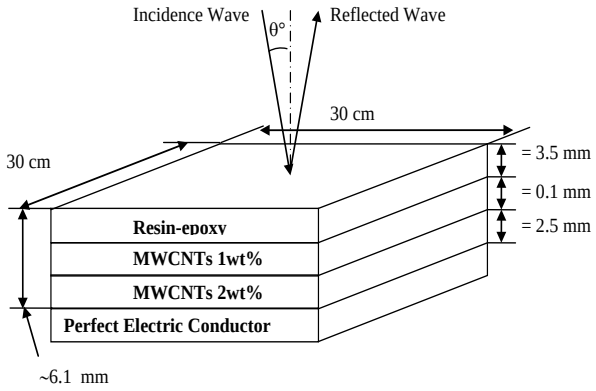

Fig. 12 RAM multilayer manufactured: Resin-epoxy MWCNTs 1 wt%, MWCNTs 2wt%, PEC

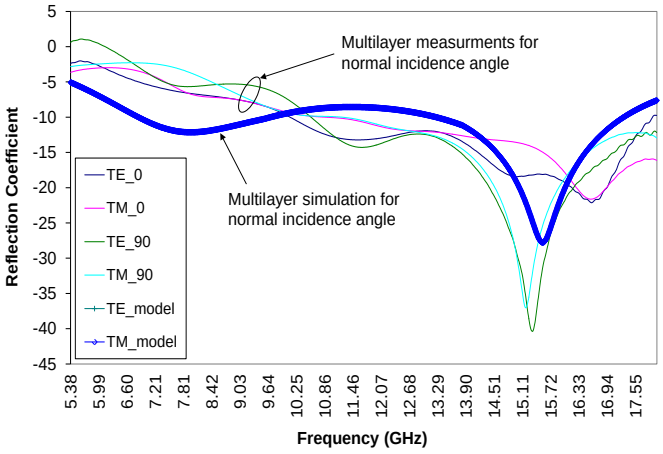

Fig. 13 RAM multilayer manufactured: resin-epoxy MWCNTs 1 wt%, MWCNTs 2wt%, PEC

To evaluate the electromagnetic reflectivity, a NRL arch measurement (bistatic reflection method), has been used [14]. In this configuration, two antennas are placed for transmitting and receiving signals respectively and the microwave reflectivity at different incident angles can be measured. Using this configuration, the reflection properties of materials, can be measured for different incident angles. It should be noted that in bistatic reflection measurements, the reflection is dependent on the polarization of the incident wave. Incident waves with parallel and perpendicular polarization usually result in different reflection coefficients. Besides, special calibration is needed for free-space bistatic reflection measurements [14]. In Fig. 14 bistatic measurement system and the tile in composite material is shown. Bistatic measurement system is here based on Agilent software 8571E (material measurement), and Agilent PNA-L vector network analyser. Antenna used are SATIMO Dual Ridge Horn SH2000 covering the frequency range 2 – 32 GHz. After the calibration of the NRL bistatic system, the reference in reflection coefficient has been taken adopting only metal plate i.e., without RAM tile. After that measurement of a known sample consisting in ECCOSORB AN73 absorber [7], has been performed in order to be aware about errors in the NRL measurement setup. Confidence of measurements was within 2 dB of interval with respect to reflection properties declared in the ECCOSORB data sheet.

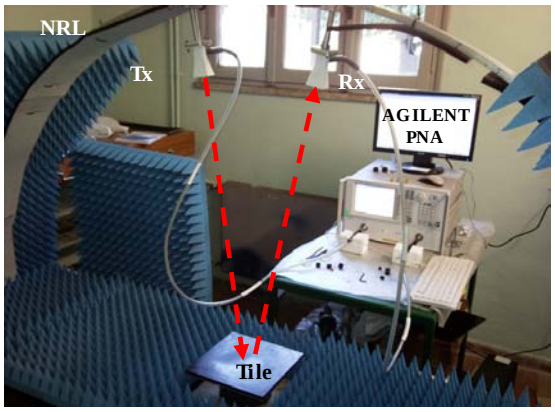

Fig. 14 Bistatic measurement system located at (www.saslab.eu)

Measurement of the manufactured RAM tile using incidence angle of 0° has been performed for TE and TM mode.

In Fig. 14 comparison between simulation of the reflection coefficient of the new manufactured RAM tile and real measurements is shown. The angle of electromagnetic wave incidence is 0°. It can be noticed that the simulated curve shows similar behaviour with respect to the measured one.

Errors and differences in simulated and measured reflection coefficient are mainly due to:

- difficulties in manufacturing RAM multilayer tile where each layer thickness ranges of about 0.5mm between its minimum to its maximum value; so the reported value represent an average value. To be aware of the manufacturing errors, in Fig. 14 we show the measurements of RAM called TE_0, TM_0, TE_90, TM_90. The numbers 0 and 90 mean that the RAM tile placed on the metal plate was rotated respectively of 0° and 90°. It can be noticed that there are some differences in the measured reflection coefficients which can be explained by errors in the manufacturing process.

- accuracy in determination of permittivity of composite materials performed using wave guide method.

- accuracy in free space measurement of reflection coefficient using bistatic method.

V. CONCLUSION

In this work modelling, optimization and manufacturing of radar absorbing materials have been discussed. The design and optimization took place using the recently introduced winning particle optimization search algorithm which has been applied to optimize the electromagnetic absorbing properties while contemporarily minimizing the overall thickness of multilayer material. Following the simulation, a large tile of radar absorbing material has been manufactured by using industrial grade of multiwall carbon nanotubes and measurement of electromagnetic reflection coefficient performed by NRL-arch. Comparison between simulation and measurement show interesting agreement. Nevertheless some errors occurred in manufacturing process which affected electromagnetic performances of manufactured radar absorbing material.

REFERENCES

[1] Lederer, P. G. *An Introduction to Radar Absorbent Materials (RAM)*, Royal Signals and Radar Establishment, Malvern, 1986.

[2] Vinoy, K. J.; Jha, R. M. *Radar Absorbing Materials: From theory to Design and Characterization*, Kluwer Academic Publishers: Boston, 1996.

[3] Knott, E. F.; Shaeffer, J. F.; Tuley, M. T. *Radar Cross Section*, 2Rev. ed ed.; Artech House: Norwood, 1993.

[4] Ruck, G. T. *Radar Cross Section Handbook*; Vol.II, Plenum Press: Newe York, 1970.

[5] Andrei Shepelev and Huib Ottens, *Horten Ho 229 Spirit of Thuringia: The Horten All-Wing Jet Fighter* ,Lan Allan Publishing Ltd, Hersham, Surrey KT12 4RG. 2006.

[6] Paul Saville, "Review of Radar Absorbing Materials", *Defence R&D Canada – Atlantic*, 2005.

[7] Davide Micheli, Carmelo Apollo, Roberto Pastore,Ramon Bueno Morlesa, Susanna Laurenzi, Mario Marchetti, "Nanostructured Composite Material for Electromagnetic Interference Shielding Applications", *Acta Astronautica, Science Direct, Elsevier*, 2011.

[8] Davide Micheli, Carmelo Apollo, Roberto Pastore, Ramon Bueno Morles, Daniele Barbera, Mario Marchetti, Gabriele Gradoni, Valter Mariani Primiani, and Franco Moglie, "Optimization of Multilayer Shields Made of Composite Nanostructured Materials", *IEEE TRANSACTIONS ON ELECTROMAGNETIC COMPATIBILITY*, 2011.

[9] Davide Micheli, *Radar Absorbing Materials and Microwave Shielding Structure Design*, LAP Lambert Academic Publishing, 2012.

[10] Davide Micheli, Roberto Pastore, Carmelo Apollo, Mario Marchetti, Gabriele Gradoni, Valter Mariani Primiani, and Franco Moglie, "Broadband Electromagnetic Absorbers using Carbon Nanostructure-Based Composites", *IEEE Transactions on Microwave Theory and Techniques*, 2011.

[11] Davide Micheli, Roberto Pastore, Carmelo Apollo, Mario Marchetti, "X-Band microwave characterization of carbon-based nanocomposite material, absorption capability comparison and RAS design simulation", *Composites Science and Technology*, 2009.

[12] J. A. Kong, *Electromagnetic Wave Theory*. New York: Wiley, 1986.

[13] J. A. Stratton, *Electromagnetic Theory*. Hoboken, NJ:Wiley-IEEE Press,. 2007.

[14] M. H. Umari, D. K. Ghodgaonkar, V. V. Varadan, and V. K. Varadan, "A free-space bistatic calibration technique for the measurement of parallel and perpendicular reflection coefficients of planar samples," *IEEE Trans. Instrum. Meas.*, vol. 40, no. 1, pp. 19–24, 1991.

Davide Micheli was born in Ancona, Italy, in 1967. He received the University degree in electronics engineering from the University of Ancona (now Università Politecnica delle Marche), Ancona, Italy, in 2001, the University degree in astronautic engineering and Ph.D. in aerospace engineering from the "Sapienza" University of Rome, Italy, in 2007 and 2011, respectively. He received the University Master degree in composites materials and nanotechnologies in aerospace applications from the "Sapienza" University of Rome, Italy, in 2012. He is currently with the Telecom Italia Laboratory (TILAB), as a Researcher with Mobile Telecommunications and Neural Networks and collaborates with "Sapienza" University of Rome, where his research activities are related to EM fields and composite materials interaction. His current research is focused on electric conductive polymers and radar-absorbing structures modeling, manufacturing and testing.

Roberto Pastore was born in Naples, Italy, in 1977. He received the University degree in Physics from the University of Studies "Federico II" of Naples, Italy, in 2003, and the University Master degree in "Composites Materials and Nanotechnologies for Aerospace Applications" from the "Sapienza" University of Rome, Italy, in 2006. He's currently on the Ph.D.Master degree in Aerospace Engineering with "Sapienza" University of Rome, where his research activities are related to carbon nanoparticles physics and nanocomposite materials characterization.

Mario Marchetti was born in San Marcello, Italy, on May 30, 1943. He received the University degree in aeronautical engineering from Milan Polytechnic, Milan, Italy, in 1972. He then joined the School of Aerospace Engineering, "Sapienza" University of Rome, Rome, Italy, where he is currently a Full Professor of the Engineering Faculty, in charge of the "Space Structures" course, the Director of the Department of Astronautic, Electric and Energetic Engineering, and is responsible for the SASLab laboratories.

Investigation of Carbon-based Aluminum Thermal Management Composites Sensitized by High-pressure Impregnation Method

Nan Jiang*, Jamie Novak

Applied Nanotech, Inc., 3006 Longhorn Blvd., Suite 107, Austin, USA

njiang@appliednanotech.net

Abstract- **Power electronic packaging highly demands the innovative light-weight heat dissipation materials with a combination of the low coefficient of thermal expansion (CTE) and the high thermal conductivity. In this study, the high-performance carbon based aluminium thermal management composite has been successfully developed by infiltrating porous carbon matrix with Al at high-pressure conditions. It is found that Al can be effectively injected into the matrix tiny pores as small as 40 – 50 nm, forming a smooth C/Al interfacial contact. The C-Al composite presents attractive thermal behaviours including high thermal conductivity (over 400 W/m-K), and a low CTE value that is smaller than 7 ppm/ K and matches well with conventional semiconductors. Also, C-Al composite is a light-weigh material which has a density only about 2.3 g/cm^3. In addition, the ceramic thin sheets can be tightly bonded to C-Al composite to form the dielectric composite plates using the same impregnation approach. The present C-Al composite is considered to be a promising candidate for a variety of thermal management applications in power electronic and photonic industrial fields.**

Keywords- C-Al Composite; Thermal Conductivity; Low CTE; Porosity; High-Pressure Impregnation

I. INTRODUCTION

Electronic and photonic devices have been pushed toward faster and higher power, with increasing demand for heat dissipation [1-3]. The average operating temperature of an electronic component is directly related to the reliability, efficiency, lifetime, and performance of the product, and over 55% of failures in electronic components are due to high operating temperatures. As the physical size of electronic components continue to shrink and become faster and more powerful, thermal management becomes more and more important. These systems require thermal management materials capable of effectively dissipating heat while maintaining physical compatibility with the package and die [4, 5]. New high performance and low cost materials are needed to address the significant deficiencies of thermal management materials today as well as for emerging applications in the future. The thermal management materials with a combination of high thermal conductivity and low CTE are highly demanded. Most traditional low CTE materials such as W/Cu, W/Mo have thermal conductivities that are no better than those of aluminium alloys, about 200 W/m-K [6, 7].

On the other hand, the outstanding thermal and mechanical properties of carbon allotropes have driven considerable interest in the development of novel thermal transfer materials. Worldwide development effort of nano-carbon heat sink composites started over a decade ago after the discovery of carbon nanotubes (CNT) and prediction of their thermal conductivity properties. These novel carbon related forms include CNT, graphene, and nano-diamond particles enhanced composites [8–10]. These composite materials are expected to be superior over others with respect to CTE, thermal conductivity and density. Meanwhile, filling the pores of a carbon matrix with metals thereby forming carbon matrix composites has also been attempted to improve the characteristics of carbon materials. As-fabricated graphitic blocks are often highly porous limiting the material's continuity and degrading the material's capability. Filling the pores of graphitic materials with metals to form carbon based metal composites has been considered to be a promising research topic [11]. However, due to the poor affinity between carbon and metals, few examples showed sufficiently filled pores or the distinct performance improvement.

In this study, we present a unique carbon based metal composite obtained through pressure injection technology that consists of a carbonaceous matrix containing 20wt% aluminium dispersed metal component. It is a sophisticated composite with low thermal expansion, high thermal conductivity and excellent thermal diffusivity.

II. EXPERIMENT

The carbonaceous matrix used for Al impregnation is produced by means of extruding a graphite/pitch mixture followed by high temperature sintering. The carbon matrix includes graphitic backbone and pores; the porosity is about 25%. A high-pressure impregnation process is used for injecting molten Al into the carbonaceous matrix. The temperature, pressure and impregnation time are optimized at about 730 ^{0}C, 100 MPa and 10 minutes, respectively. The material composition and microstructure are evaluated by transmission electron microscopy (TEM) and scanning electron microscopy (SEM) equipped with the dispersive x-ray spectroscopy (EDS). The thermal properties are investigated by laser flash measurement (KEM LFA-502), and a PoreMaster 60 porosimeter was employed to exams material porosity and pore size distribution before and after Al impregnation.

III. RESULTS AND DISCUSSION

The material developed in this study begins with a porous graphitic carbon. The final form consists of carbonaceous matrix of which most of pores are filled by aluminium. Fig. 1 is a typical image showing C-Al composite appearance. The black contrast area is metric carbon, in which the white domains are aluminium-filled pores. The C-Al composite fabricated in this study is in a block shape and can have a maximum dimension of 250 mm x 200 mm x 150 mm. This kind of C-Al composite has a nice machinability, and

fabrication of complicated shape parts is feasible as revelled in the inset of Fig. 1, wherein C-Al composite has been processed into a fin-type heat sink parts.

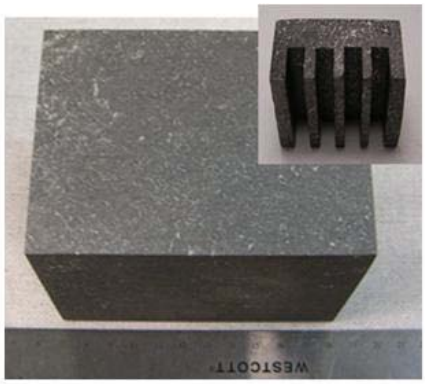

Fig. 1 Images of C-Al composite and a machined heat sink parts (inset)

Table Ⅰ outlines the major thermal properties of the C-Al composite. Using a carbon matrix as the majority component in the composite allows achieving a small CTE (no more than 7 ppm/K) providing compatibility with commonly used semiconductor materials such as Si, GaN and GaAs. The low CTE feature offers the opportunity for direct attachment of electronic compoents (even bare chips) on the composite materal without cracking or delamination of the semconduct orcompoents due to thermal expansion mismatch. It is feasible to manufacture the material with anisotropy in the alignment of the graphitic carbon structure.

TABLE I THERMAL PROPERTIES OF C-AL COMPOSITE

Orientation	Unit	X-Y (Normal o Extrusion Direction)	Z (Extrusion Direction)
Thermal Diffusivity	Cm^2/Sec	1.25	2.55
Thermal Conductivity	W/m-K	200	425
CTE	Ppm/K	2.2	7
Specific Heat	J/Gk	0.75	0.75

For example, when the carbon starting material is extruded the C-Al composite has a thermal conductivity of 425 W/m-K in the extrusion direction (Z direction).

This compares favorabily to bulk Al and Cu thermal conductivies of 237 W/m-K and 390 W/m-K, respectively. In general, a substance's thermal diffusivity is an important factor contributing to fast heat transfer and rapid temperature equilibrium, helping eliminate the "hot spots" generated in the electronic system. The Z direction thermal diffusivity is 2.55cm^2/sec, which is about 2.5 – 3 times higher than that of Cu or Al. Although the composites is anisotropic, their thermal diffusivity is still higher than that of Al and Cu along X-Y directions (normal to the extrusion direction), and the thermal conductivity of X-Y directions can also be as high as those of Al alloys. Another advantage of using carbon as a base material is the relativly low mass density (2.3 g/cm^3) which is lighter than Al (ρ = 2.7 g/cm^3). Low density is an important consideration [12] in aerospace and automotive applications where saving just a few grams can be the only route to maximize the performance of the overall system. The combination of the improved thermal performance and lighter weight for a C-Al composite material is advantageous for a wide variety of thermal management applications.

Thermal management composites must rely on several factors to achieve good thermal conduction, including: (i) high thermal conductivity of the parent materials; (ii) lack of voids and cavities in the material and (iii) in many cases, creation of well contacted interface between the two parent materials. The C–Al composite has the potential to achieve excellent thermal conductivity since both aluminium and graphitic carbon have high thermal conductivity values. However, the last two criteria offer much room for improvement.

In order to well understand the nature of the material's outstanding thermal performance, C-Al composite's microstructure and C/Al interface have been investigated. Fig. 2 shows a SEM image (upper), and the corresponding EDS mappings of carbon element (middle) and aluminium element (lower) taken from the C-Al composite. Fig. 2 reveals that Al (as indicated by arrows) is infused into the irregular shape pores with few voids visible. This point has also been evidenced by EDS mapping pictures, wherein the contours of Al and C regions exactly match with each other. These images tell for sure that Al has been impregnated into carbonaceous matrix very well; and it fills pores and perfectly integrates with surrounding carbon matrix.

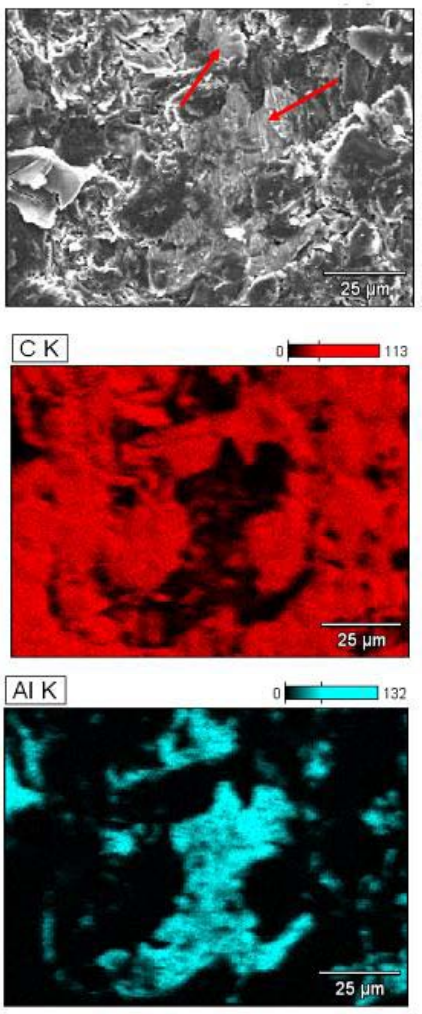

Fig. 2 A typical SEM image of the C-Al composite (upper) and the corresponding EDS mappings of carbon (middle) and aluminum (lower)

Material's porosity and pore size distribution before and after Al impregnation were studied using a PoreMaster 60 porosimeter system which allows measuring a wide range pore size distribution from nanometer up to sub-millimetre. The graphitic carbon matrix before Al impregnation has a porosity of about 25 vol. %, and after impregnation the total pore volume has been greatly reduced. The formed C-Al composite has porosity of only about 8 vol. %, namely near 70% initial pores are filled by Al. As the result, the material density increases from the 1.75 g/cm^3 to 2.30 g/cm^3, and the C-Al composite consists of about 80 wt% of carbon and 20 wt % of Al. Comparing Fig. 3a and 3b, it is not difficult to find Al impregnation killed most pores that are greater 40 - 50 nm, but for the pores smaller than 20 - 30 nm, changes are minor, meaning the filling effectiveness for this impregnation process can extend to 40 – 50 nm tiny pores. We call this nanoscale filling as "nano-infiltration".

As mentioned above, it is well known for composite material synthesis, control over the interface between the matrix and the foreign fillers are especially important and represent one of the key factors affecting the final material's properties. In general, carbon materials and molten metal have poor wettability and affinity to one another. This creates a situation where the molten alloy does not want to wet the surface of the carbon. In other words, the high surface tension of the metal results in insufficient filling of the porous graphitic materials. This results in loss of contact between the two materials leaving voids and poor thermal performance. Careful control over the interface between the aluminium and carbon and the specify process parameters can overcome these limitations.

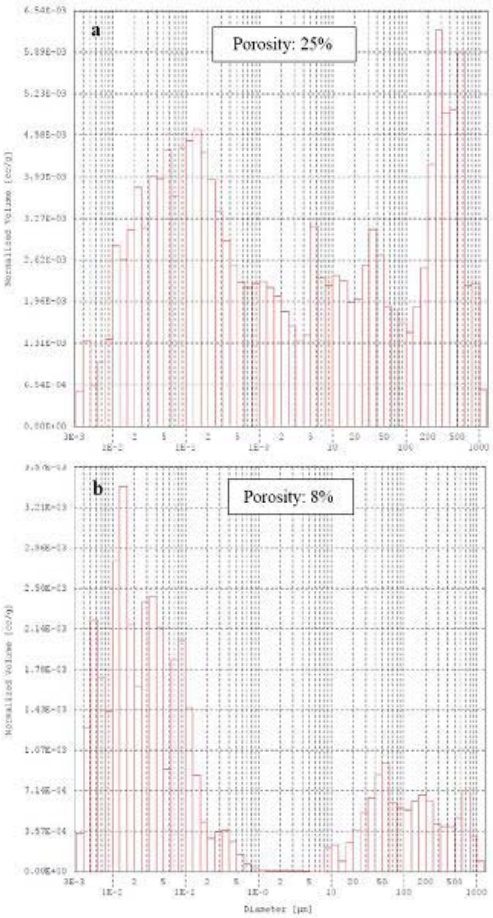

Fig. 3 The pore size distribution before (a) and after (b) Al impregnation

As one can observe from Fig. 4, the high-pressure impregnation allows aluminium to create a well matched interface at the nano-scale dimensions including contact angle and flatness, where the size of interfacial voids or slits (as noted by arrows) has been successfully suppress to less than 100 nm forming a closely contacted interface between the carbon phase and Al phase that ensures the heat flow can be smoothly conveyed from one phase to another phase. An organic combination of smooth interface contact, nano-infiltration, and the intrinsic advantages of Al and graphitic carbon is just the reason accounting for C-Al composite's excellent thermal behaviours.

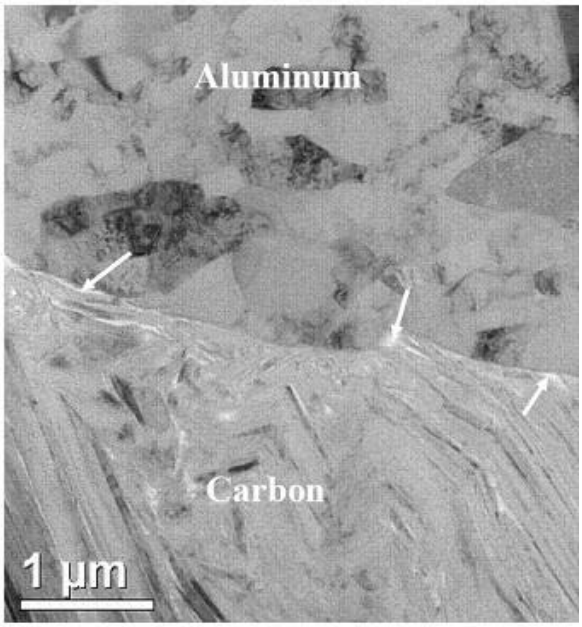

Fig. 4 A typical TEM image showing the C/Al interface
The interfacial nano-voids and slits are indicated by arrows

In this study, to further extend the composites' application, we also developed the electrically insulating C-Al plate by attaching a ceramic sheet to the outer surface of a thermal management composite plate. In the areas such as IGBT (insulated gate bipolar transistor) or CPV (concentrating photovoltaic) cells, the electrically insulating materials with exceptional thermal performance are required. One normal way to provide electrical isolation is to adhere ceramic insulators onto traditional thermal management material surfaces using adhesives such as epoxy. However, the low thermal conductivity of epoxy can significantly raise the cross-sectional thermal resistance and impede the heat transport. In this study, we present a novel approach by which the insulating ceramic sheet can be directly bonded to the composite surface during the high pressure impregnation manufacturing process. This results in an electrically insulating material without using organic adhesives that could potentially reduce thermal performance. A carbon matrix plate and a ceramic sheet were previously stacked together, and during the high pressure impregnation process, as the molten Al is injected into the porous carbon to form composite, a part of molten Al can also be injected into the gap between that carbon plate and ceramic sheet, tightly connecting the two parts into one body as revealed in Fig. 5, where a silicon nitride sheet is bonded on C-Al composite. The combination of these materials provides a facile route to excellent adhesion. One can expect outstanding cross-sectional heat transport behaviours due to eliminating the

organic adhesives and even better thermal performances by further thinning the ceramic sheet thickness.

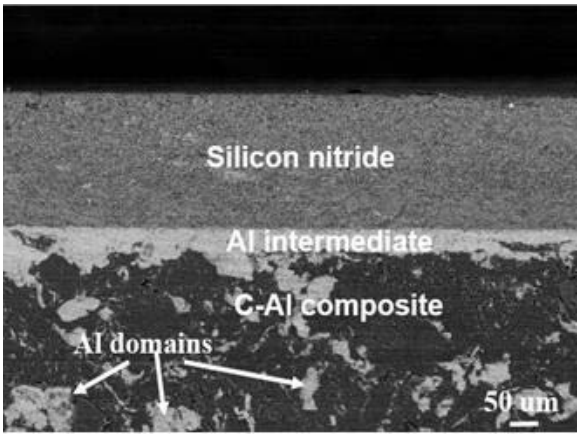

Fig. 5 SEM image of the C-Al composite with a silicon nitride dielectric sheet bonded on the top

IV. CONCLUSIONS

The C-Al thermal management composite material has been developed by means of high-pressure impregnation process.

At the optimized process conditions, molten Al can be effectively injected into the pores that can be as small as 40 – 50 nm in the carbon matrix creating a close contact at C/Al interface.

After impregnation, near 70% initial pores are occupied by Al fillers. The C-Al composite presents a low CTE, a high thermal conductivity and an excellent thermal diffusivity. Smooth interface contact, nano-infiltration, and the intrinsic advantages of Al and graphitic carbon are considered to be the three key factors accounting for C-Al composite's excellent thermal behaviours. The C-Al composite plates with the surface electrically insulating ceramic sheets have also been successfully produced by the same impregnation approach without using any foreign adhesive materials.

REFERENCES

[1] Luedtke A., 2004, Adv. Eng. Mater., 6, 142.
[2] Mahajan R., Chiu C. P., and Chrysler G., 2006, Proc. IEEE, 94, 1476.
[3] Lin W., Zhang R., Moon K. S., and Wong C. P., 2010, Carbon , 48, 107.
[4] Zweben C., 2005, Adv. Mater. Process, 163, 33.
[5] Zweben C., 2006, Power Electron. Technol., 2, 40.
[6] Lostetter, A., Barlow F., and Elshabini, A., 1998 Adv. Microelectronics, 25, 25.
[7] Pintsuk G., Brunings S. E., Linke J., Smid J., and Xue L., 2003, Fusion Eng. Design, 66 – 68, 237.
[8] Chu K., Guo H., Jia C., Yin F., Zhang X., Liang X., and Chen H., 2010, Nanoscale Res. Lett., 5, 868.
[9] Goyal V., and Balandin A. A., 2012, Appl. Phys. Lett., 100, 073113.
[10] Correia J. B.,; Livramento V., Shohoji, N., Tresso E., Yamamoto. K, Taguchi T., Hanada K., and Osawa, E., 2008, Mater. Sci. Forum, 744, 443.
[11] Weeks J. R., and Sommer J. L., 1998, US Patent 5834115.
[12] Moores K. A., and Joshi Y. K., 2001, Future Circuits Intl., 7, 45.